Matter

CellPress
OPEN ACCESS

Article

Computationally Driven Discovery of Layered Quinary Oxychalcogenides: Potential *p*-Type Transparent Conductors?

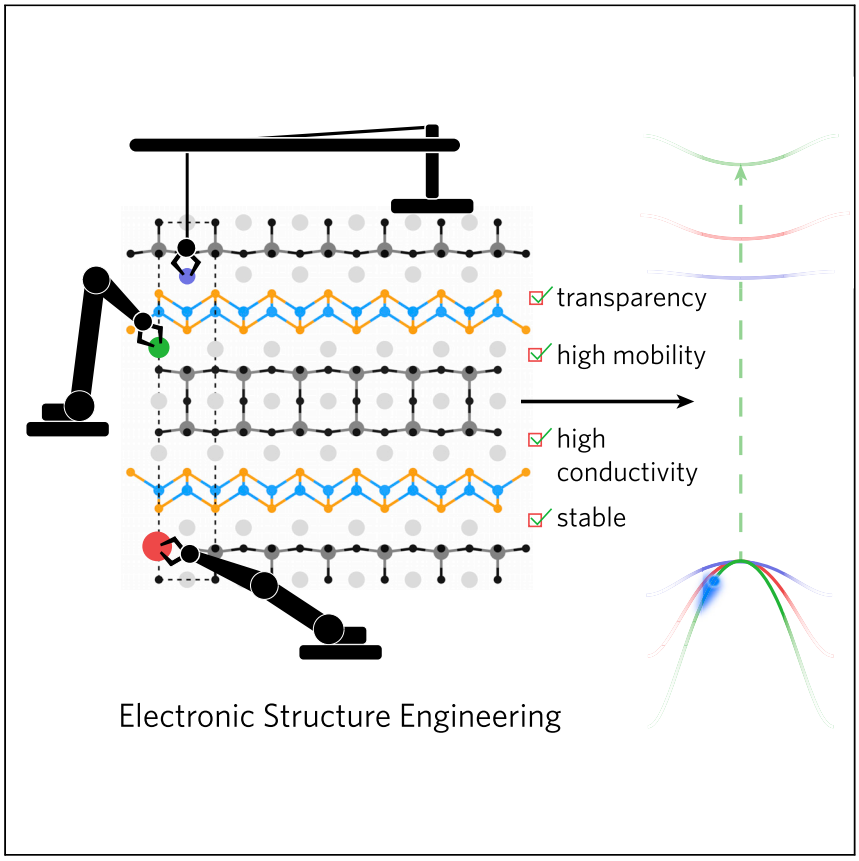

Benjamin A.D. Williamson, Gregory J. Limburn, Graeme W. Watson, Geoffrey Hyett, David O. Scanlon

benjamin.williamson.10@ucl.ac.uk (B.A.D.W.)
g.hyett@soton.ac.uk (G.H.)
d.scanlon@ucl.ac.uk (D.O.S.)

HIGHLIGHTS

24 compounds were screened based on the $[Cu_2S_2][A_3M_2O_5]$ (I4/mmm) structure

Of the compounds, $[Cu_2S_2][Ba_3Sc_2O_5]$ was predicted to be the optimum *p*-type TC

$[Cu_2S_2][Ba_3Sc_2O_5]$ had a theoretical conductivity of 2,058 S cm^{-1} at 1 × 10^{21} cm^{-3}

Successful synthesis of $[Cu_2S_2][Ba_3Sc_2O_5]$ was achieved experimentally

The realization of transparent electronics is hindered by the lack of a suitable high-mobility *p*-type transparent conductor (TC). This work used *ab initio* simulations to search for a *p*-type TC based on the layered oxychalcogenide $[Cu_2S_2][A_3M_2O_5]$ structure. The main result of this study was the discovery of the optimum *p*-type oxychalcogenide TC, $[Cu_2S_2][Ba_3Sc_2O_5]$, predicted to have a higher optical band gap, better hole mobility, and greater stability than its parent compound $[Cu_2S_2][Ba_3Sc_2O_5]$; this was verified experimentally.

Benchmark
First qualification/assessment of material properties and/or performance

Williamson et al., Matter *3*, 1–23
September 2, 2020
Published by Elsevier Inc.
https://doi.org/10.1016/j.matt.2020.05.020

Please cite this article in press as: Williamson et al., Computationally Driven Discovery of Layered Quinary Oxychalcogenides: Potential *p*-Type Transparent Conductors?, Matter (2020), https://doi.org/10.1016/j.matt.2020.05.020

Matter

CellPress
OPEN ACCESS

Article

Computationally Driven Discovery of Layered Quinary Oxychalcogenides: Potential *p*-Type Transparent Conductors?

Benjamin A.D. Williamson,[1,2,6,*] Gregory J. Limburn,[3] Graeme W. Watson,[4] Geoffrey Hyett,[3,*] and David O. Scanlon[1,2,5,*]

SUMMARY

***n*-type transparent conductors (TCs) are key materials in the modern optoelectronics industry. Despite years of research, the development of a high-performance *p*-type TC has lagged far behind that of its *n*-type counterparts, delaying the advent of "transparent electronics"-based p-n junctions. Here, we propose the layered oxysulfide $[Cu_2S_2][Sr_3Sc_2O_5]$ as a structural motif for discovering *p*-type TCs. We have used density functional theory to screen 24 compositions based on this motif in terms of their thermodynamic and dynamic stability and their electronic structure, thus predicting two *p*-type TCs and eight other stable systems with semiconductor properties. Following our predictions, we have successfully synthesized our best candidate *p*-type TC, $[Cu_2S_2][Ba_3Sc_2O_5]$, which displays structural and optical properties that validate our computational models. It is expected that the design principles emanating from this analysis will move the field closer to the realization of a high figure-of-merit *p*-type TC.**

INTRODUCTION

Transparent conductors (TCs) are ubiquitous in modern life with applications ranging from portable electronics to gas sensing and photovoltaics.[1] At present the field is dominated by high-mobility, high-conductivity *n*-type materials such as In_2O_3,[2,3] SnO_2,[4–7] ZnO,[8,9] and $BaSnO_3$.[10,11] Equivalent *p*-type materials, however, remain elusive despite decades of dedicated research.[12–15] Should a high-performance *p*-type TC be found, the fabrication of transparent p-n junctions would bring about the realization of transparent electronics as well as provide a wider range of materials for use as electrodes in current devices such as photovoltaics.[12,13,16–18]

Multiple design strategies have been created to formulate increased *p*-type conductivity while retaining a large optical band gap ($E_g^{opt} > 3.1$ eV). In particular these are: (1) *p*-type doping of *n*-type TCs;[15,19–27] (2) $(n-1)d^{10}ns^2$ metal oxides incorporating main group cations such as Sn^{2+}, Pb^{2+}, and Bi^{3+}; (3) spinel oxides such as $ZnCo_2O_4$;[28,29] and (4) the "chemical modulation of the valence band" (CMVB) formulated by Hosono and coworkers based on $CuAlO_2$.[30]

Details of these methods are described at length by Zhang et al.[1] However, to date the most robust and successful method for designing *p*-type TCs is arguably the CMVB method. Hosono's group reported that the delafossite $CuAlO_2$ possessed the Cu *3d*–O *2p* mixing present in the valence band of Cu_2O while retaining the wider band gap of Al_2O_3.[30] From this study they established design rules that

Progress and Potential

This work has predicted and experimentally realized the *p*-type transparent conductor $[Cu_2S_2][Ba_3Sc_2O_5]$, and at the same time has developed design principles for layered oxychalcogenide materials of this structure type. The layered oxychalcogenide materials offer a large configurational space of potentially stable compounds with tunable functional properties for a wide range of applications. The longer-term ambitions of the research are to use the combined methods of density functional theory and experiments to search for and understand further layered oxychalcogenide structure types and configurations for different semiconductor applications. This research has the potential to affect the types of electronic devices by bringing us closer to the realism of transparent electronics. The research presented will also further the development of applications for which transparent conductors are essential, such as solar cells.

involved the preferential mixing of a d^{10} closed-shell cation such as Cu^{1+} with O 2*p* states at the valence band maximum (VBM). The effect of this hybridization is that the typically polaronic nature of holes at the VBM are delocalized, lowering the ionization potential while promoting favorable dispersion. This is also achieved via tetrahedral coordination of oxygen by reducing the non-bonding states by distributing the electrons along the four σ bonds.[31] To maintain high optical transparency, Cu must be closed shell (Cu^{1+}, d^{10}) and spatially separated from other Cu atoms in order to avoid both intra- and inter-atomic *d*–*d* excitations (coloration).

Other delafossite materials such as $CuGaO_2$,[32–35] $CuInO_2$,[32,35] $CuCrO_2$,[36] $CuBO_2$,[34,37,38] $CuScO_2$,[32,35,39] and $SrCu_2O_2$[40,41] have all been studied, where in each case the *p*-type conductivities were typically several orders of magnitude lower than *n*-type TCs despite being transparent to visible light. To date the highest reported conductivity for a delafossite TC is for Mg-doped $CuCrO_2$ ($CuCrO_2$:Mg) of 220 S cm^{-1}.[36] This typically arises from the deep nature of the acceptor defects in these materials hindering degenerate conductivity.[42,43]

A natural progression is to extend down the chalcogenides to S and Se. It has been shown that the band gap decreases from Cu_2O to Cu_2S to Cu_2Se, yet with an increase in conductivity.[44–46] This is indicative of more dispersive VBMs at lower ionization potentials and, thus, a greater propensity for *p*-type degeneracy. LaCuOS and LaCuOSe are two layered oxychalcogenides that have been shown to possess the 50:50 Cu *3d*–Ch *2p* mixing at the VBM while retaining relatively wide band gaps (LaCuOS = 3.1 eV, LaCuOSe = 2.8 eV[17,47]). Despite the lower band gap, Mg-doped LaCuOSe displays far higher *p*-type conductivities (910 S cm^{-1}[48]) than Sr-doped LaCuOS (2.6 × 10^{-1} S cm^{-1}[49]) due to the increased covalency of Cu *3d* with Se *4p* over S *3p*.

One of the most promising *p*-type TCs in recent years is the layered oxychalcogenide $[Cu_2S_2][Sr_3Sc_2O_5]$,[50] which possesses a 3.1-eV band gap, high reported hole mobilities of 150 cm^2 V^{-1} s^{-1}, and undoped conductivities of 2.8 S cm^{-1} despite the low carrier concentrations of 10^{17} cm^{-3}.[51] This structure comprises alternating $[Cu_2S_2]^{2-}$ and perovskite-like $[Sr_3Sc_2O_5]^{2+}$ layers as shown in Figure 1. Hybrid functional density functional theory (DFT) calculations showed a desirable electronic structure where *p*-type conductivity originates from the $[Cu_2S_2]^{2-}$ layer while the $[Sr_3Sc_2O_5]^{2+}$ layer accounts for the wide band gap.[37]

As a quinary material the $[Cu_2S_2][Sr_3Sc_2O_5]$ structure can be used as a prototype, allowing for a large configurational space of *p*-type transparent conducting materials and, thus, a greater potential for success in finding materials with low hole effective mass and degenerately dopable. This method of computationally driven design has been successfully implemented in advancing the search for high-mobility transparent *p*-type semiconductors in previous studies.[52–54] Combining this with technological breakthroughs in thin-film and solid-state synthesis procedures allow for the fabrication of "designer" layered compounds; thus, greater control is achievable, allowing previously unobtainable metastable or difficult-to-synthesize layered compounds to be realized.[55–58] In this work, using cation substitution in the oxide layer, we computationally predict eight layered oxysulfides with optical band gaps spanning the range 0.78–3.24 eV. Based on our predicted properties, our proposed champion TC, $[Cu_2S_2][Ba_3Sc_2O_5]$, is successfully synthesized, showing excellent agreement with our calculated structural and optical properties.

[1]Department of Chemistry, University College London, 20 Gordon Street, London WC1H 0AJ, UK

[2]Thomas Young Centre, University College London, Gower Street, London WC1E 6BT, UK

[3]Department of Chemistry, University of Southampton, Southampton SO17 1BJ, UK

[4]School of Chemistry and CRANN, Trinity College Dublin, The University of Dublin, College Green, Dublin 2, Ireland

[5]Diamond Light Source Ltd., Diamond House, Harwell Science and Innovation Campus, Didcot, Oxfordshire OX11 0DE, UK

[6]Lead Contact

*Correspondence: benjamin.williamson.10@ucl.ac.uk (B.A.D.W.), g.hyett@soton.ac.uk (G.H.), d.scanlon@ucl.ac.uk (D.O.S.)

https://doi.org/10.1016/j.matt.2020.05.020

Please cite this article in press as: Williamson et al., Computationally Driven Discovery of Layered Quinary Oxychalcogenides: Potential *p*-Type Transparent Conductors?, Matter (2020), https://doi.org/10.1016/j.matt.2020.05.020

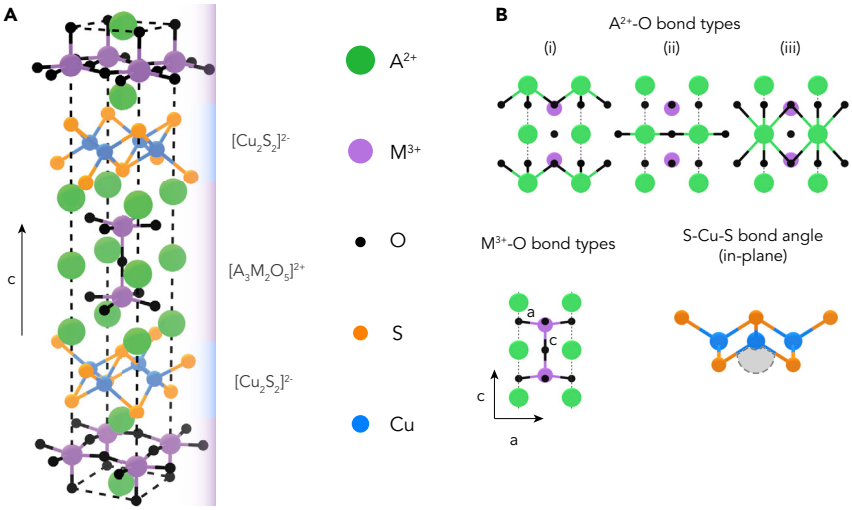

Figure 1. An Overview of the $[Cu_2S_2][A_3M_2O_5]$ Structure and Associated Bond Types and Angles

(A) The $[Cu_2S_2][Sr_3Sc_2O_5]$ and the crystal structure as viewed along the [100] direction where Cu = blue, S = orange, A^{2+} = green, M^{3+} = purple, and O = black.

(B) The different bond types for A^{2+}–O and M^{3+}–O and the S–Cu–S in-plane bond angle. In this structure the Cu atoms are tetrahedrally bonded to S within the $[Cu_2S_2]^{2+}$ layer while within the $[A_3M_2O_5]^{2+}$ layer, there exist square-based pyramids of M^{3+} and O. The A^{2+} cations are generally coordinated in a square anti-prismatic configuration either with 8 oxygens or 4 oxygens and 4 sulfurs.

RESULTS

Computational Results

Thermodynamic Stability Screening

The calculations in this work involved forming variations of the $[Cu_2S_2][A_3M_2O_5]$ structure (tetragonal, I4/mmm) and stoichiometry where A = **Sr**,Ca,Ba,Mg and M = **Sc**,Al,Ga,In,Y,La, resulting in 24 compounds. To simplify the nomenclature, we use the convention "AB" in this work, e.g., $[Cu_2S_2][Sr_3Sc_2O_5]$ is "SrSc" and $[Cu_2S_2][Ba_3Al_2O_5]$ is "BaAl." The thermodynamic stability of the 24 compounds at 0 K was calculated relative to ~313 (geometry relaxed) competing stable phases taken from the Inorganic Crystal Structures Database.[59] A stability criterion was established from the energy above the convex hull (E above hull) and ranges from 0 to 0.07 eV $atom^{-1}$ following work by Ceder and coworkers.[60] An absolute maximum can also be applied based upon the synthesis temperature (k_BT, where T ≈ 800°C) in Liu et al.,[51] which gives an E above hull of ~0.09 eV $atom^{-1}$. The E above hull values for each compound are tabulated in Table S2 and those within the stability window are shown in Figure 2. Of the 24 compounds calculated, 10 were identified within this stability criterion: SrAl, SrGa, SrSc, CaAl, CaGa, CaSc, BaAl, BaGa, BaSc, and BaIn. Among these, the parent compound SrSc possesses an E above hull of 5×10^{-4} eV $atom^{-1}$ and as such is predicted to be stable (within the errors of DFT), while CaSc, BaAl, and BaIn are predicted to be metastable with energies of 0.05, 0.07, and 0.01 eV $atom^{-1}$, respectively. CaSc, BaAl, and BaIn are expected to form but may not be phase pure when synthesized and, as such, other competing phases may be present. All compounds where A^{2+} = Mg and M^{3+} = Y and La were found to be unstable. To simplify the discussion in this work, we discuss only the compounds with both A^{2+} = Ca, Sr, Ba and M^{3+} = Al, Ga, Sc in the main text. The structural parameters, band structure, optical absorption, and phonons for BaIn can be found in Supplementary Information (Table S5 and Figure S1).

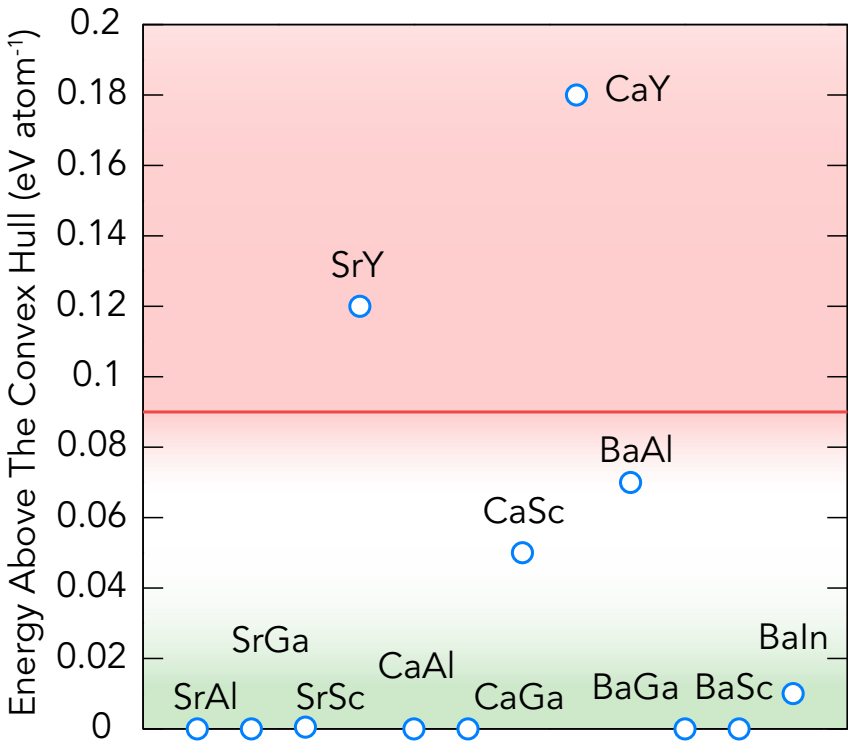

Figure 2. Depiction of the Stable and Metastable Compounds with Respect to the Stability Criterion 0–0.09 eV atom^{-1}

The green area is the predicted "stable" region (0–0.02 eV atom^{-1}), the white region depicts the area of metastability (0.02–0.09 eV atom^{-1}), and the red region is the unstable region (>0.09 eV atom^{-1}). The graph predicts ten potentially stable variations on the $[Cu_2S_2][Sr_3Sc_2O_5]$ structure.

Geometric and Structural Properties

All thermodynamically stable compounds displayed the same I4/mmm crystal structure as the parent compound after relaxation.

Cell Parameters

Table 1 gives the calculated structural parameters for all the stable compounds using HSE06. The calculated lattice parameters and bond lengths for the parent compound, SrSc, are in excellent agreement with the experimental values,[50] showing the efficacy of HSE06 to predict the structural properties of all 24 compounds. As expected, when increasing the size of both A^{2+} and M^{3+} cations, the cell parameters, volumes, and bond lengths all increase while retaining the I4/mmm crystal symmetry. In terms of volume change, within the Al, Ga, and Sc compounds (Ca → Ba) an increase in volume by around 20%, 18%, and 16% is seen for each subgroup, respectively, while the *a*/*c* parameters expand by around 5%/10%, 4%/10%, and 3%/9%, respectively.

$[Cu_2S_2]^{2-}$ Layer. Previous HSE06 studies carried out on SrSc[61] as well as LaCuOS and LaCuOSe[47] showed that the $[Cu_2Ch_2]^{2-}$ layer is responsible for the electronic states that form the VBM and is thus important in terms of *p*-type conductivity. Figure 3 displays the change in valence-band-related bond lengths and angles comparative with increasing *a* parameter. For each M^{3+} group, expectedly there is a proportional increase in Cu–Cu, Cu–S, and A^{2+}–S distances as well as S–Cu–S bond angles (in-plane) compared with *a*. In general, a direct comparison of the basal lattice parameter (*a*) with the individual electronic and structural properties

Please cite this article in press as: Williamson et al., Computationally Driven Discovery of Layered Quinary Oxychalcogenides: Potential *p*-Type Transparent Conductors?, Matter (2020), https://doi.org/10.1016/j.matt.2020.05.020

Table 1. Structural Parameters and Bond Lengths for All Stable Predicted Compounds Calculated Using HSE06

Compound	*a* (Å)	*c* (Å)	Volume (Å)	$d_{Cu–Cu}$ (Å)	$d_{Cu–S}$ (Å)	$<_{S–Cu–S}$ (°)	$d_{M(3+)–O}$ (c,a) (Å)	$d_{A(2+)–O}$ (i,ii,iii) (Å)	$d_{A(2+)–S}$ (Å)
CaAl	3.71	25.66	353.84	2.63	2.39	101.5	1.78, 1.88	2.36, 2.63, 2.78	2.97
SrAl	3.79	26.77	384.47	2.68	2.4	104.13	1.78, 1.92	2.51, 2.68, 2.82	3
BaAl	3.89	28.26	427.34	2.75	2.41	107.95	1.80, 1.97	2.69, 2.75, 2.89	3.21
CaGa	3.83	25.66	376.07	2.71	2.39	105.3	1.87, 1.93	2.37, 2.71, 2.90	3.04
SrGa	3.88	26.72	401.88	2.74	2.42	106.85	1.87, 1.96	2.53, 2.74, 2.91	3.11
BaGa	3.97	28.22	445.08	2.81	2.41	110.4	1.91, 2.01	2.70, 2.81, 2.99	3.25
CaSc	4.02	25.25	407.69	2.85	2.43	111.67	1.98, 2.03	2.41, 2.84, 3.01	3.16
SrSc	4.08	26.07	433.45	2.89	2.45	114.55	1.97, 2.05	2.55, 2.88, 3.04	3.2
SrSc (experimental)	4.08	25.99	433.45	2.88	2.49	110	1.91, 2.07	2.51, 2.88, 3.05	3.18
BaSc	4.15	27.44	472.11	2.94	2.45	115.37	1.99, 2.09	2.70, 2.93, 3.07	3.32

The compounds are ordered in groups relating to M^{3+} and within these groups in terms of increasing cell lattice parameter (*a*) or increasing A^{2+} cation. The different A^{2+}–O and M^{3+}–O bond types are shown in Figure 1, and the S–Cu–S bond angles refer to "in-plane" bond angles (where the S and Cu atoms occur in the same *ac* plane as each other).

of the system can be applied. An increased Cu–Cu distance is typically preferred to avoid *d*−*d* transitions known to hamper the transparency of Cu–O-based systems.[12] In this work the Cu–Cu distances increase from 2.63 Å for CaAl to 2.94 Å for BaSc, suggesting that the latter will be least likely to suffer colorations due to *d*−*d* transitions. The Cu–S distances tend to plateau for the Sr and Ba compounds within each M^{3+} group and have a minimum bond length of 2.39 Å for CaAl and a maximum of 2.45 Å for BaSc. It is likely that the Cu–S bond length restrains the systems from expanding further and, hence, partially dictates the stability of the $[Cu_2S_2][A_3M_2O_5]$ structure to accommodate the different variations. The results herein lie within the typical range of other copper sulfide-based materials such as Cu_2S (~2.27–2.35 Å)[62,63] as well as the layered oxysulfide LaCuOS (~2.42 Å).[49] Judging from the increase in bond length from LaCuOS to LaCuOSe and even LaCuOTe[49,64,65] (2.42 → 2.52 → 2.66 Å), selenide- or telluride-based $[Cu_2S_2][A_3M_2O_5]$ systems may be able to accommodate the increasing cell size and, hence, larger A^{2+} and M^{3+} cations such as Y or La.

The S–Cu–S bond angles (in-plane, where the S and Cu atoms are in the *ac* plane) increase with *a* producing a "concertina" effect on the $[Cu_2S_2]^{2-}$ layer. The calculated HSE06 value for SrSc (114.55°) is in reasonable agreement with experiment, overestimating slightly by ~5°.[50] This linear trend, however, is broken slightly from SrSc to BaSc, whereby it is possible that a limit to the bond angle is occurring; any larger cells would likely become strained, favoring either a different crystal structure or the use of Se or Te within the $[Cu_2S_2]^{2-}$ layer. Cu_2S is known to have an S–Cu–S bond angle of 109.5°[62,63] and LaCuOS possesses one of 108.63°.[49]

The A^{2+}–S bond lengths were also calculated to establish an "inter-layer spacing" between the $[Cu_2S_2]^{2-}$ and $[Sr_3Sc_2O_5]^{2+}$ layers. In general, from Ca → Sr → Ba the increase is linear with respect to *a* and, to an extent, between the different M^{3+} groups. The maximum percentage increase within the Al, Ga, and Sc groups is 8%, 7%, and 5%, respectively.

$[A_3M_2O_5]^{2+}$ Layer. The average A^{2+}–O and M^{3+}–O bond lengths increase linearly relative to both *a* and *c* lattice parameters. Predictably the M^{3+}–O bond lengths are correlated with the change in their respective cell directions; however, for the A^{2+}–O bond lengths the analysis can be split into the effect on the *xy* and *z* directions

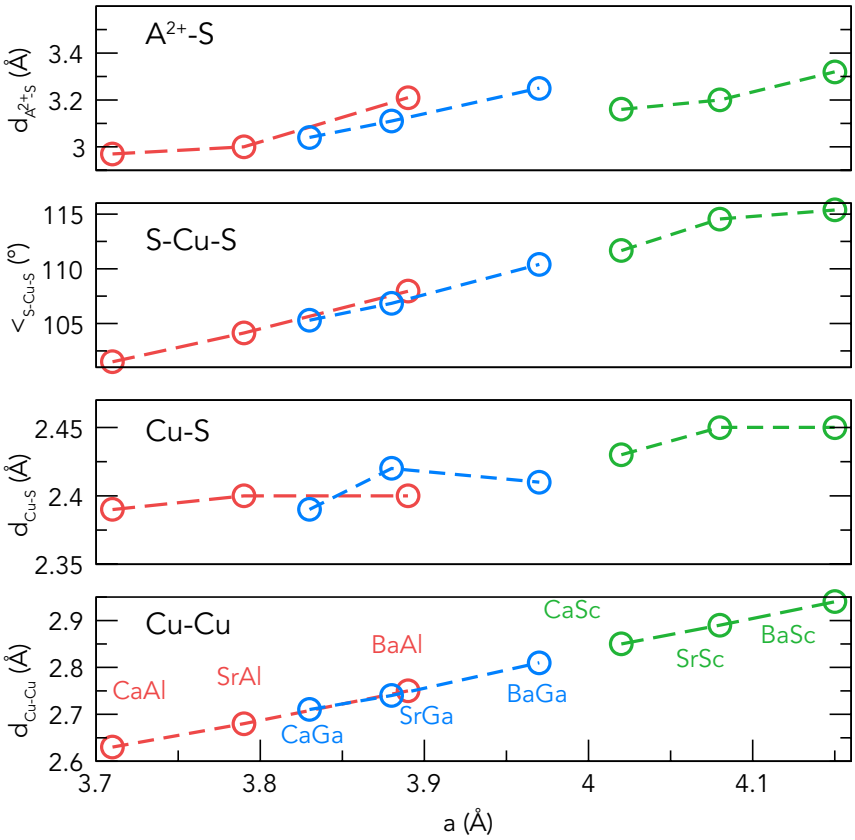

Figure 3. Bond Lengths and Angles Related to the Valence Band ($[Cu_2S_2]^{2-}$ Layer), Cu–Cu, Cu–S, S–Cu–S, and A^{2+}–S with Respect to Increasing Basal Lattice Parameter

due to the tetrahedral bonding of A^{2+} (the different bond types are shown in Figure 1). Although the bonds in the *xy* plane increase linearly with *a*, the bond lengths in the *z* direction show little change between increasing A^{2+} cation and, thus, *c* parameter.

Electronic and Optical Properties

Density of States. Figures 4A–4C show the total and partial density of states (DOS) for SrAl, SrGa, and SrSc, respectively, which will be used as representatives of each M^{3+} group in this analysis (the full plots for all nine compounds are shown in Figure S2). Also given are the percentage of states at the VBM together with valence band widths (upper "uninterrupted" valence bands between −12 eV and 0 eV) in Table S6 and the conduction band minimum (CBM) in Table S7.

Within each M^{3+} group the composition of the upper valence band remains the same, with only the valence band widths changing among the groups. In general, the valence band widths decrease with increasing A^{2+} cation radius and are inversely proportional to the S–Cu–S angle. It can be surmised, therefore, that the more obtuse the S–Cu–S angle, the smaller the valence bandwidth; however, as shown in Figure 4 this is not necessarily the case where both Al and Ga *s* + *p* states are present from ~−10 eV to −7 eV. From ~−7 eV to −5 eV in SrAl and SrGa, significant mixing between O *p*, S *p*, Cu *d*, and Al/Ga *p* states is seen. For SrSc, M^{3+} *s* states are not seen in this region, instead being replaced with mixing between O *p*, S *p*, Cu *d*, and Sc *d* states. After this point the compounds become very similar, with a

Please cite this article in press as: Williamson et al., Computationally Driven Discovery of Layered Quinary Oxychalcogenides: Potential *p*-Type Transparent Conductors?, Matter (2020), https://doi.org/10.1016/j.matt.2020.05.020

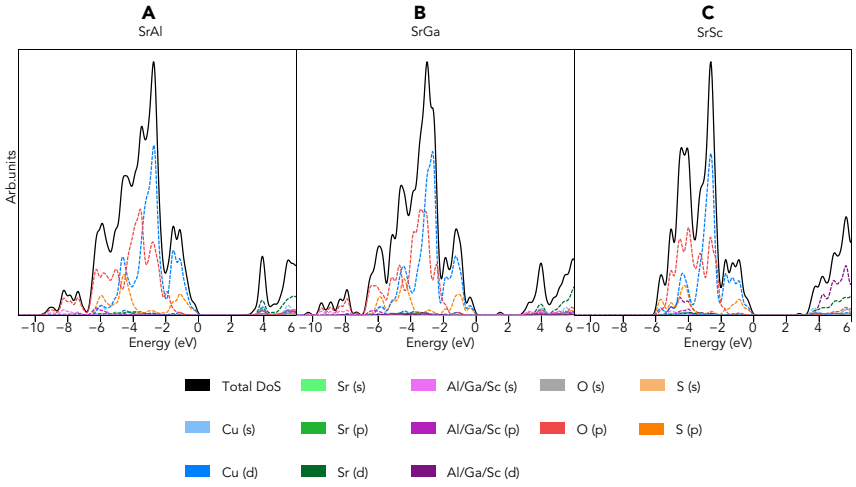

Figure 4. Density of States

Representative density of states (DOS) for the different groups, SrAl (A), SrGa (B), and the parent compound: SrSc (C). In each example the VBM is set to 0 eV. Full partial and total DOS for all other compounds can be found in Figure S2.

large proportion of the DOS belonging to Cu *d* mixed with O *p* states in a nearly 50:50 ratio from ~−3 eV to ~−2 eV.

From −2 eV to the VBM (0 eV), Cu *d* states hybridize with S *p* states over O *p* almost exclusively in ~55:~41 Cu/S ratio with negligible contributions from Cu *p*, Sr *p* + *d*, and O *p* states (Table S6). These results are similar to previous HSE06 calculations on SrSc[61] and LaCuOCh (where Ch = S, Se, Te).[66]

The states at the CBM (Table S7) vary more widely with composition for each group of compounds. Within the aluminum compounds, it is clear that a hybridization between the Cu *s*, S *s*, Al *s*, and O *s* states generally make up the CBM. The influence of increasing A^{2+} cation radii plays a significant role increasing the Al *s* character of the CBM from 5% to 30%, together with O *s* + *p* while decreasing the overall contribution from Cu and S states from 58% in SrAl to just 25% in BaAl. In CaAl, a significant mixing of Ca *s* states is present at the CBM, which may be likely due to possessing the smallest A^{2+}–S bond length (2.97 Å).

The gallium systems display predominantly Ga *s* and O *s* mixing with a markedly reduced presence of Cu *s* and S *s* states compared with the aluminum compounds. This large change in M^{3+} "*s*" character between the Al and Ga compounds is likely due to the increasingly penetrating *s* orbitals down group 13, an effect that can be observed in the lower-lying CBM from InN to AlN.[67] As with the Al, an increase in the Ga *s* states from CaGa to BaGa are observed from 51% to 68%, respectively.

In both SrAl and SrGa (Figures 4A and 4B), from around 2.7 eV to the peak at 4 eV the conduction band consists of increasing M^{3+} *s* and O *p* and Sr *d* states, while from 4 eV to 6 eV the latter states increase further with some O, Cu, and M^{3+} states present.

The CBMs of the scandium compounds differ from those of the aluminum and gallium compounds in that negligible quantities of Sc states are observed. The CBM is predominantly Cu *s* and S *s* + *p* with significant mixing from A^{2+} states. From CaSc to BaSc the Cu *s* states increase from 21% to 34%, in contrast to the Al and

Please cite this article in press as: Williamson et al., Computationally Driven Discovery of Layered Quinary Oxychalcogenides: Potential *p*-Type Transparent Conductors?, Matter (2020), https://doi.org/10.1016/j.matt.2020.05.020

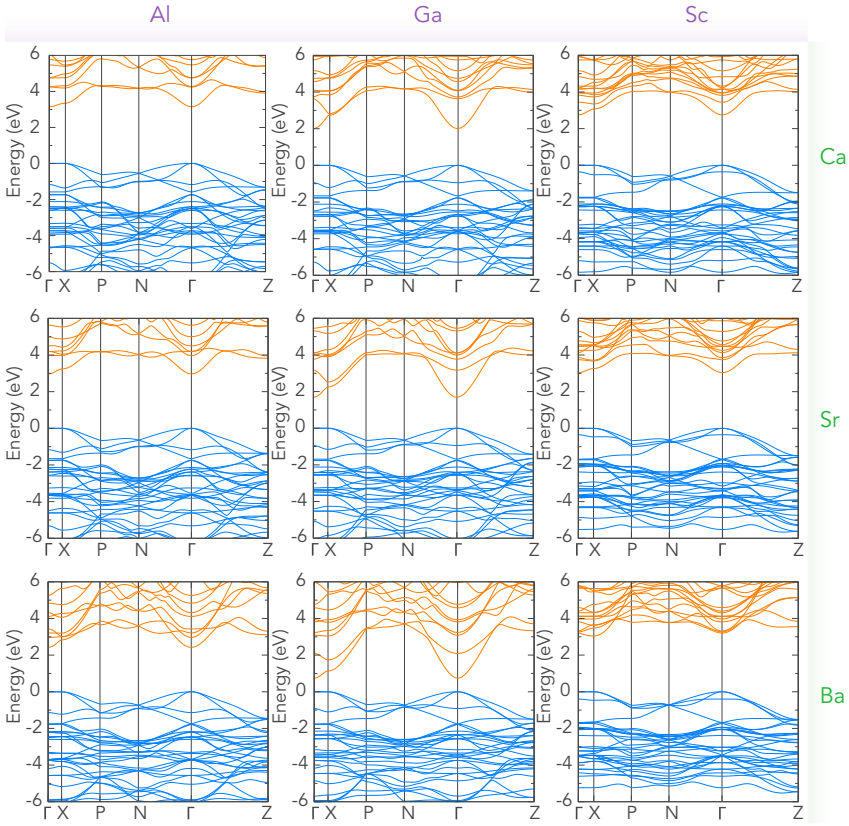

Figure 5. Combined Band Structures for the Stable and Metastable $[Cu_2S_2][A_3M_2O_5]$ Compounds Calculated Using the HSE06 Functional

The band structures are arrayed in a grid such that the top left corresponds to CaAl and the bottom right to BaSc. In the stable examples, the valence bands are depicted in blue and the conduction bands in orange, where the VBM is set to 0 eV. The band structures are ordered in terms of increasing A^{2+} cation ionic radii (Ca → Sr → Ba) and in terms of increasing M^{3+} cation radii (Al → Ga → Sc).

Ga compounds where increasing A^{2+} resulted in fewer Cu and S states at the CBM. Between CaSc and SrSc, a reduction in A^{2+} *s* states is observed. BaSc shows that the Ba *d* states dominate at the CBM with no S *s* or *p* states (as with CaSc and SrSc). This is likely due to the decreased Ba–Cu distance over Ca–Sc and Sr–Sc, respectively, due to the "concertina" effect of the $[Cu_2S_2]^{2-}$ layer and, thus, a more compact unit cell. In SrSc, the conduction band from the CBM to 6 eV consists of an increasing proportion of Sr *d* and Sc *d* states. Toward 6 eV an increased hybridization with O *p*, S *p*, and Cu *s* states is seen.

Band Structure and Optical Gap. The band structures of all stable $[Cu_2S_2][A_3M_2O_5]$ compounds are presented in Figure 5 and the direct, indirect, and optical band gaps together with hole and electron effective masses at the VBM and CBM, respectively, are shown in Table 2. The value for the optical band gap is taken from the α^2 value (analogous to the Tauc relation: $(\alpha\ h\nu)^2$) in the absorption spectra compiled for each of the nine compounds in Figure S3.

From our calculations, 3 of the 24 $[Cu_2S_2][A_3M_2O_5]$ compounds, CaAl, SrSc, and BaSc, are found to be transparent, with optical band gaps of 3.17, 3.06, and 3.24 eV, respectively. The optical band gap for SrSc (3.06 eV) is in accordance with that

Please cite this article in press as: Williamson et al., Computationally Driven Discovery of Layered Quinary Oxychalcogenides: Potential *p*-Type Transparent Conductors?, Matter (2020), https://doi.org/10.1016/j.matt.2020.05.020

Table 2. Fundamental Direct and Indirect Band Gaps Together with the Optical Band Gap for the $[Cu_2S_2][A_3M_2O_5]$ Compounds Alongside the Various Effective Masses for Both the VBM and CBM

Compound	E_g^{fund} (Direct)	E_g^{fund} (Indirect)	E_g^{opt}	Γ-X/m_e			Γ-N/m_e			Γ-Z/m_e	
				VBM	CBM	VBM (h)	VBM (l)	CBM	VBM (h)	VBM (l)	CBM
CaAl	3.14	–	3.17	85.3	0.52	4.54	0.37	0.36	0.81	0.55	0.31
SrAl	2.97	–	3	44.98	0.39	3.05	0.36	0.34	0.75	0.55	0.34
BaAl	2.42	–	2.46	17.34	0.32	2.37	0.37	0.33	0.72	0.56	0.33
CaGa	2.01	–	2.03	85.31	0.23	3.92	0.37	0.25	0.7	0.61	0.26
SrGa	1.69	–	1.71	45.14	0.24	2.7	0.35	0.23	0.62	0.59	0.23
BaGa	0.74	–	0.78	31.3	0.25	2.21	0.33	0.2	0.6	0.52	0.2
CaSc	2.75	–	2.78	22.16	0.37	3.12	0.45	0.34	0.77	0.76	0.33
SrSc	3.04	–	3.06	47.42	0.45	2.5	0.45	0.35	0.75	0.73	0.35
BaSc	3.24	3.04 (Γ-X)	3.24	28.54	0.95 (X-Γ)	1.9	0.43	0.35 (X-P)	0.72	0.63	–

The optical gap value is taken from α^2 as seen in Figure S3. The direct gaps for BaSc are displayed for the direct transition at X and the direct transition at Γ.

seen in the experiment by Liu et al., who observed a band gap around 3.1 eV.[51] It is also possible that SrAl will be transparent; however, coloring or haze may arise due to the 3.00-eV optical band gap. In general the optical band gaps correspond to the direct fundamental band gap at Γ, but for BaSc this is not the case. BaSc is the only compound to possess an indirect fundamental band gap where the VBM and CBM are located at Γ and X, respectively; however, the difference in energy is around 2×10^{-3} eV between the two points. The indirect and direct band gaps at X are, however, disallowed transitions due to the *d*-orbital nature of both the VBM (Cu *d*) and CBM (Ba *d*); thus, the origin of the optical band gap arises from the direct gap at Γ (3.20 eV), which is an allowed transition.

Figure 6A shows the change in direct fundamental band gap as a function of *a* parameter. In both Al and Ga compounds the band gap shrinks as a function of increasing cell size, which can be attributed to the increasing M^{3+} *s* character at the CBM from Ca to Ba. Due to the larger penetration of the Ga 4*s* states over Al 3*s*, the CBM is lowered yet further in the gallium compounds. The lower band gap, however, does allow for a greater dispersion at the CBM and thus a lower electron effective mass, as can be clearly seen in the band structures in Figure 5 and Table 2.

Conversely, the scandium compounds, which see barely any Sc-related states at the CBM, show a widening of the fundamental band gap with increasing *a* parameter. The band gap, therefore, is highly sensitive to the different states at the band maxima and minima, and no one rule can be used to describe all compounds.

To possess high hole mobilities and thus produce degenerate *p*-type conductivity, the effective masses at the VBM must be low (<0.5 m_e). For all nine compounds a band degeneracy exists at the VBM such that one can calculate both a "heavy" and "light" effective mass (the Γ–X direction is amalgamated into one value due to the heavy nature of the holes in this direction). In the Γ–N and Γ–Z directions, SrSc experiences heavy effective masses of 2.50 m_e and 0.75 m_e and light hole effective masses of 0.45 m_e and 0.73 m_e, respectively, corroborating the high mobilities (150 $cm^2\ V^{-1}\ s^{-1}$[51]) seen at low carrier concentrations in powder samples of SrSc.

Figure 6B shows the trends of the hole effective masses as a function of *a* parameter for the Γ–N and Γ–Z directions for each M^{3+} group. The heavy effective masses in the

Please cite this article in press as: Williamson et al., Computationally Driven Discovery of Layered Quinary Oxychalcogenides: Potential *p*-Type Transparent Conductors?, Matter (2020), https://doi.org/10.1016/j.matt.2020.05.020

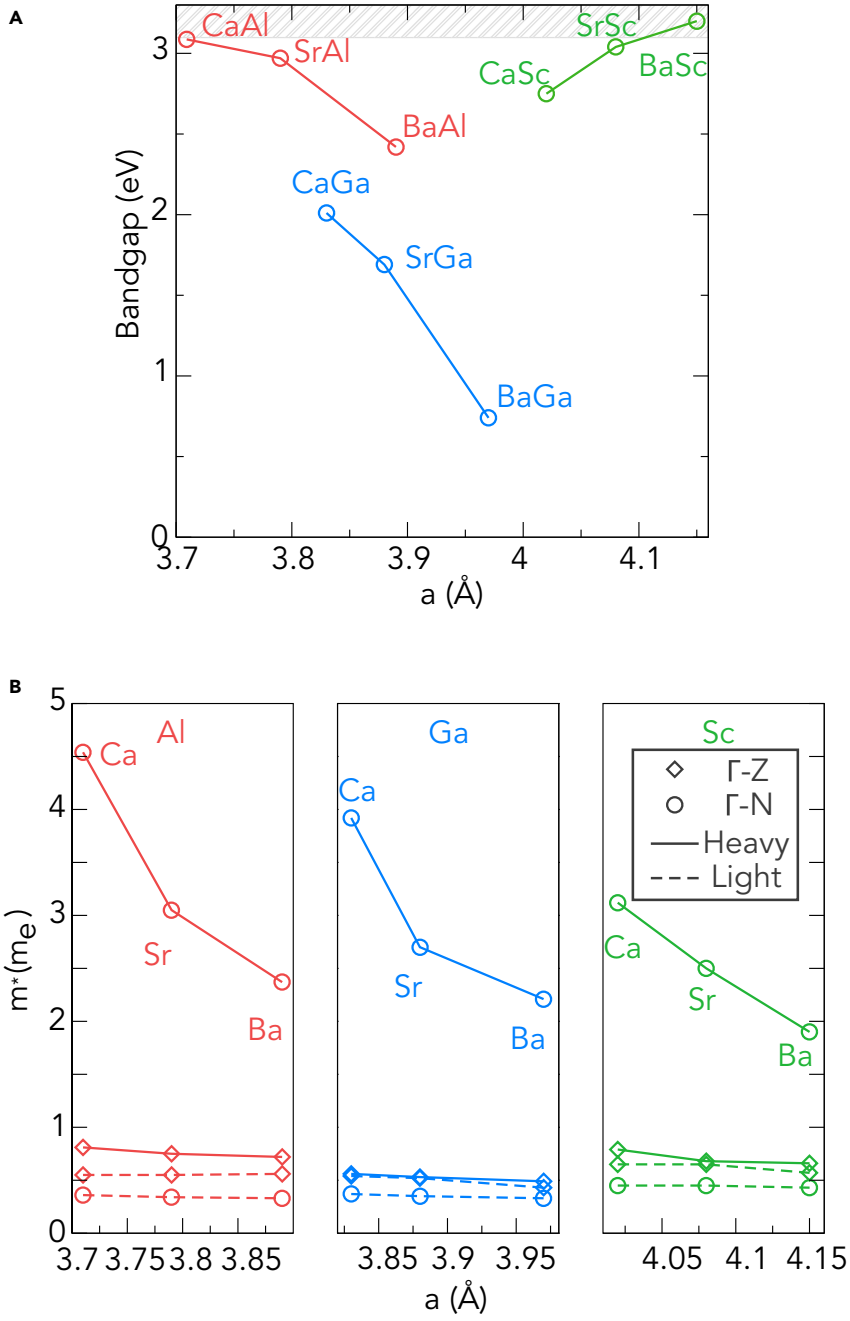

Figure 6. The Effect of Lattice Parameter *a* on the Electronic Structure

(A) The direct fundamental band gap as a function of increasing *a* parameter. The hashed gray region corresponds to the visible light transparency region.

(B) The VBM hole effective mass as a function of increasing *a* parameter.

Γ–N direction decrease with increasing *a*, giving maximum values of 4.54 m_e, 3.92 m_e, and 3.12 m_e for Al, Ga, and Sc, respectively and minimum values of 2.37 m_e, 2.21 m_e, and 1.90 m_e, respectively, with the latter belonging to BaSc.

The light hole effective masses in the Γ–N direction remain relatively constant in both the Al and Sc compounds with average effective masses of 0.37 m_e and 0.34

Please cite this article in press as: Williamson et al., Computationally Driven Discovery of Layered Quinary Oxychalcogenides: Potential *p*-Type Transparent Conductors?, Matter (2020), https://doi.org/10.1016/j.matt.2020.05.020

m_e, respectively. The gallium compounds undergo a slight decrease in magnitude from 0.37 m_e for CaGa to 0.33 m_e for BaGa. In contrast to the heavy hole effective masses seen in this direction, the Sc compounds display slightly higher effective masses compared with the Al and Ga compounds.

In the Γ–Z direction, both heavy and light hole effective masses are low. From CaAl to BaAl, the heavy effective masses decrease from 0.81 m_e to 0.72 m_e while the light hole masses remain around ~0.55 m_e. In the gallium compounds, a decrease is seen in both the heavy and light effective masses with the lowest observed for BaGa (0.52 m_e). Both heavy and light hole effective masses remain fairly similar in the scandium compounds with the exception of BaSc, which displays a heavy and light effective mass of 0.72 m_e and 0.63 m_e, respectively. From CaSc to BaSc the effective masses decrease with increasing *a* parameter for both the heavy and light holes.

From Γ–X, however, the hole effective masses are very high (17.34–85.30 m_e) and easily visualized by the lack of dispersion in the band structures. This is likely due to a lack of overlap between the Cu *d* and S *p* tetrahedra in the $[Cu_2S_2]^{2-}$ layers. The Γ–X direction corresponds to the *xy* plane and hence with a "flattening" of this layer due to the more obtuse S–Cu–S angles, so it can be expected that a better overlap between Cu and S will occur, thus lowering hole effective masses in this direction. This effect is certainly observed in the aluminum and gallium compounds where the effective masse reduces from 85.31 m_e to 17.34 m_e and 85.31 m_e to 31.30 m_e, respectively. The scandium compounds, however, do not follow the same trend, with the largest values being attributed to SrSc. The very high mobilities in the experiment by Liu et al.,[51] however, suggest it is likely that the Γ–X direction does not limit the mobilities as much as the Γ–N and Γ–Z directions.

In general, the electron effective masses in all directions decrease as a function of increasing *a* parameter. Due to the lower-lying CBM in the gallium compounds, the lowest electron effective mass is seen for BaGa with an average effective mass of 0.20 m_e, competitive with the industry standard *n*-type TCs such as In_2O_3 (0.22 m_e).[68] In the scandium compounds, the trend is broken due to the Ba *d* states forming an indirect band gap with the CBM at X. Of the stable compounds, therefore, BaSc possesses the highest electron effective masses of 0.95 m_e (X–Γ) and 0.35 m_e (X–P).

Dynamic Stability

To further analyze the dynamic stability of the predicted structures, we calculated the phonon dispersion curves, shown in Figures 7A–7C for CaAl, SrSc, and BaSc, respectively (and for the nine compounds in Figure S6).

It was found that for the three TC compounds (BaSc, SrSc, and CaAl) no imaginary modes appeared at Γ, indicating that each structure is dynamically stable; however, in both the SrSc and CaAl structures imaginary acoustic modes appear around N and Z for SrSc and just at N for CaAl, indicating that these might not be the ground-state structures at lower temperatures.

These results can be indicative of potential structural distortions to reach another structural phase that is lower in energy. However, the I4/mmm structure may likely be stable at room temperature, as is the case with SrSc.

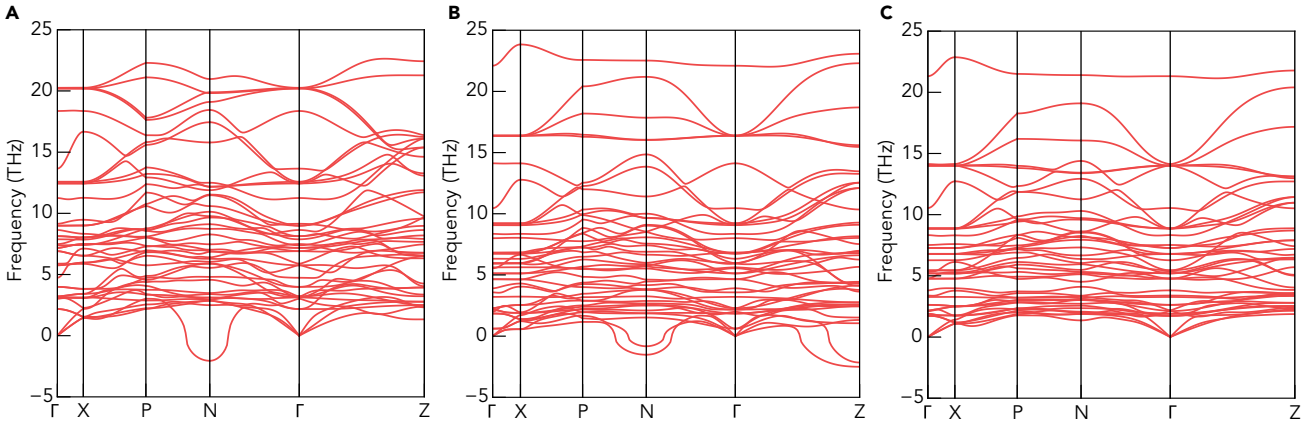

Figure 7. Phonon Dispersion and Dynamic Stability

The phonon dispersion for CaAl (A), SrSc (B), and BaSc (C). SrSc and BaSc are both in the I4/mmm while CaAl is in the C2/m space group. Phonon dispersion spectra can be found for all compounds in Figure S6.

Calculated Conductivity

Using Boltzmann transport theory, the *p*-type conductivities for BaSc, SrSc, and CaAl were calculated at varying carrier concentrations using HSE06. From our calculations we find that BaSc possesses the highest *p*-type conductivity of 2,058 S cm^{-1} followed by CaAl (1,767 S cm^{-1}) and SrSc (1,673 S cm^{-1}) at a carrier density of 1×10^{21} cm^{-3} (Figure 8). These results compare well with the average hole effective masses showing that BaSc should have a higher mobility (and thus a larger conductivity) compared with CaAl and SrSc. In our experiment, powder samples of $[Cu_2S_2][Sr_3Sc_2O_5]$ displayed undoped conductivities of 2.8 S cm^{-1} from a carrier concentration of $\sim 10^{17}$ cm^{-3}.[51] From the BoltzTraP calculations we find that for a carrier concentration of 1×10^{18} cm^{-3}, SrSc has a conductivity of 2.03 S cm^{-1}. It is likely that for a powder sample, the accuracy of the carrier concentrations determined from the Hall effect may be questioned due to the grain boundaries, although these results help to validate the use of BoltzTraP to determine the conductivity of these compounds.

Importantly, these values are significantly larger than that of the highest reported *p*-type conductivity seen for Mg-doped (220 S cm^{-1}) $CuCrO_2$,[36] making BaSc potentially the highest performing *p*-type TC to date. Analysis of the defect chemistry of BaSc would, however, be required to determine whether a high carrier concentration can be reached for BaSc and the optimum dopant necessary to facilitate this. For comparison, the calculated conductivities for well-known *n*-type TCs are presented in Figure 8 alongside experimental values for Sn-doped In_2O_3, Al/Ga-doped ZnO, and F/Sb/Ta-doped SnO_2 at carrier concentrations of $\sim 1 \times 10^{21}$ cm^{-3}. Although the *p*-type conductivities are not of the same order as the *n*-type TCs, the significant enhancement in conductivity from BaSc drastically closes the gap.

Experimental Results

To validate our predictions, we prepared a sample of $[Cu_2S_2][Ba_3Sc_2O_5]$ by direct combination of BaO, Sc_2O_3, Cu_2S, and BaS. This yielded a light-brown powder with a crystalline diffraction pattern.

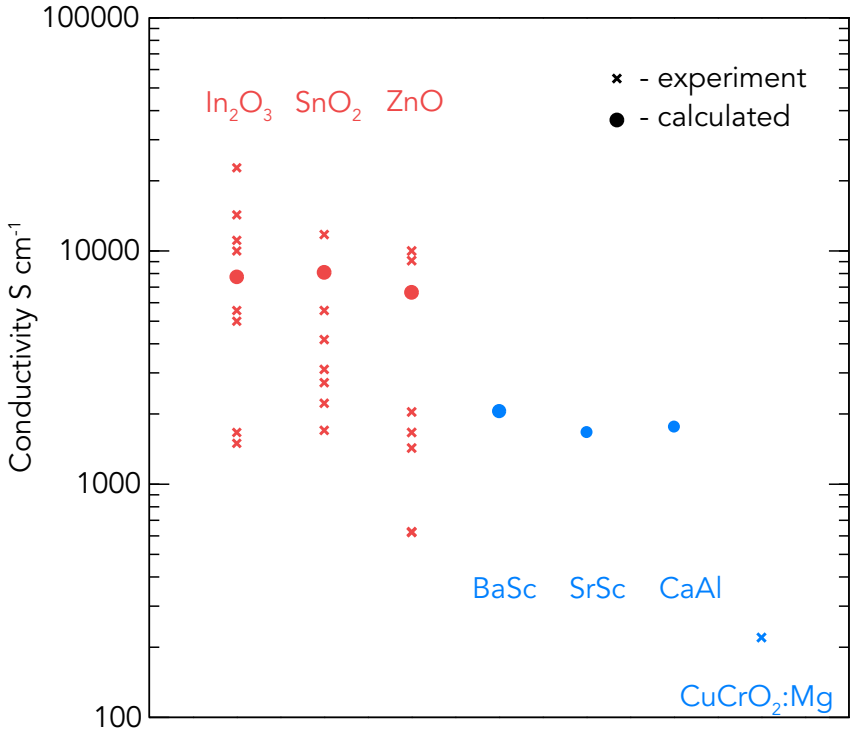

Figure 8. Calculated and Experimental Conductivities for *n*-type TCs (In_2O_3, SnO_2, ZnO), Shown in Red, and the *p*-type TCs, Shown in Blue

$CuCrO_2$:Mg refers to Mg-doped $CuCrO_2$. The values are taken for a doping level of ~1 × 10^{21} cm^{-3}. References are included in Table S8.

X-Ray Diffraction

The powder X-ray diffraction (PXRD) pattern of $[Cu_2S_2][Ba_3Sc_2O_5]$ is shown in Figure 9. A Rietveld refinement was carried out against these data using a starting model based on the previously reported and assumed isostructural $[Cu_2S_2][Sr_3Sc_2O_5]$, but with replacement of strontium ions with barium ions and an appropriate expansion in lattice parameters. Refinement of this model against the data was carried out with refinement of the background function, the Lorentzian and Gaussian components of pseudo-Voight peak-profile functions, the lattice parameters, the atomic positions, and their isotropic displacements. The refinement confirmed that $[Cu_2S_2][Ba_3Sc_2O_5]$ was single-phase crystallizing in the tetragonal I4/mmm space group with lattice parameters of a = 4.14462(2) Å and c = 27.12390(8) Å, with a good fit to the data with χ^2 = 2.938 and Rp = 7.80%. The final structural model is given in Table S9. All the structural parameters are given in Table 3.

All structural properties are in excellent agreement with the calculated HSE06 values by <2% with a slight overestimation of the c direction.

Optical Absorption

Spectroscopic diffuse reflection data were recorded on the sample of $[Cu_2S_2][Ba_3Sc_2O_5]$ and used to produce a Tauc plot, which can be seen in Figure 10. This shows a strong absorption that can be attributed to a direct band gap of 3.24 eV. This puts the band gap in the UV range, and therefore we would predict that the material should be transparent, which is contradicted by the observed light-brown color of the powder. However, there is an additional, less intense feature in the plot that

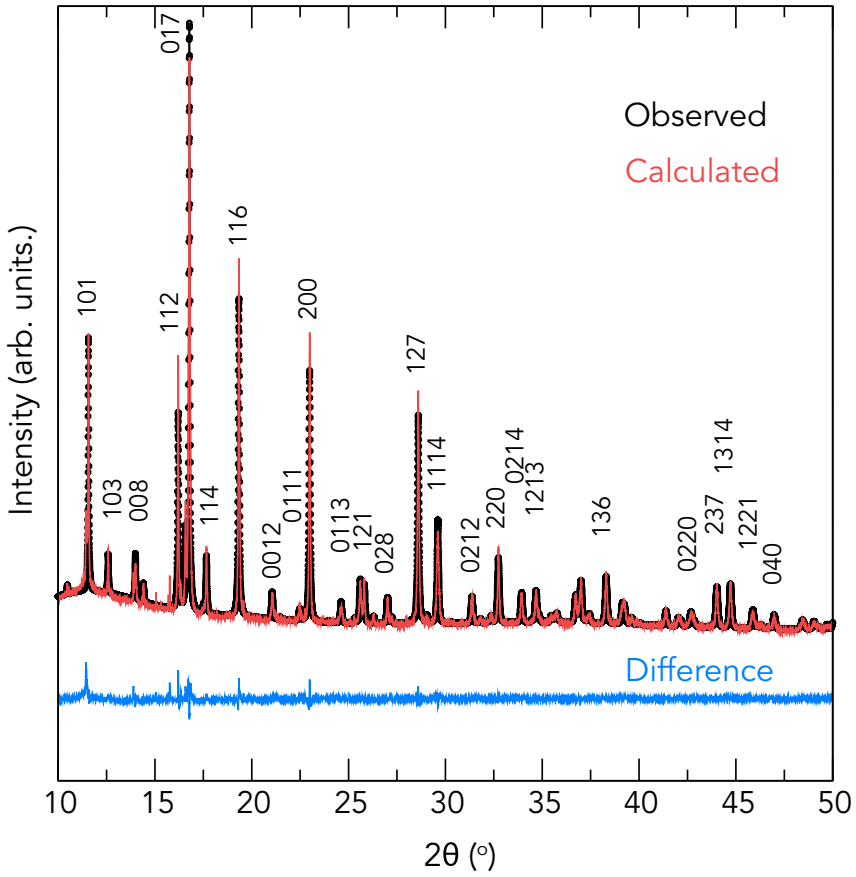

Figure 9. Indexed Synchrotron Powder X-ray Diffraction Pattern Collected Using the I11 Beamline at the Diamond Light Source, with a Wavelength of 0.82603 Å

Black crosses represent the observed diffraction data, the red line the calculated diffraction pattern, and blue line the difference between these values. This plot shows the final Rietveld refinement model of $[Cu_2S_2][Ba_3Sc_2O_5]$. Note that different scales are used on the intensity and difference plots. The peak at ~11.44° arises from diluting emulsion added to the sample to reduce X-ray absorption.

can be related to a band gap of 2.26 eV, which is more consistent with the observed color. The origin of this is still not clear, but could be due to an amorphous impurity or *d–d* transitions within Cu-related defects.

DISCUSSION

From our analysis, two potential *p*-type TCs have been predicted using hybrid functional DFT. These compounds are CaAl and BaSc with optical band gaps of 3.17 eV and 3.24 eV, respectively. The synthesis of BaSc powders confirms the predictions gained from DFT, in particular the wide optical band gap. From the structural analysis, a clear trend can be seen based on the *a* lattice parameter. With increasing cell volume, a narrowing of the $[Cu_2S_2]^{2-}$ layer is seen to influence the curvature and width of the valence critical to the electronic properties.

In the delafossite Cu^{1+} oxides, a large Cu–Cu distance is necessary to suppress *d*−*d* transitions; however, it was also found that due to the polaronic nature of the conductivity, a smaller Cu–Cu distance is preferable to reduce the "hopping" distance. This can be seen in the higher undoped conductivities observed for $CuBO_2$ over

Please cite this article in press as: Williamson et al., Computationally Driven Discovery of Layered Quinary Oxychalcogenides: Potential *p*-Type Transparent Conductors?, Matter (2020), https://doi.org/10.1016/j.matt.2020.05.020

Table 3. Structural Parameters, Bond Lengths, and Optical Band Gap for the BaSc Powders

Parameters	Experiment	HSE06
a (Å)	4.14	4.15
c (Å)	27.12	27.44
$d_{Cu–Cu}$ (Å)	2.93	2.94
$d_{Cu–S}$ (Å)	2.44	2.45
$<_{S–Cu–S}$ (°)	116.07	115.37
$d_{M(3+)–O}$ (*c*,*a*) (Å)	2.00, 2.08	1.99, 2.09
$d_{A(2+)–O}$ (i,ii,iii) (Å)	2.71, 2.93, 3.04	2.70, 2.93, 3.07
$d_{A(2+)–S}$ (Å)	3.3	3.32
E_g^{opt} (eV)	3.24	3.24

$CuAlO_2$.[46,61] We find that in the $[Cu_2S_2][A_3M_2O_5]$ materials, an extended Cu–Cu distance is correlated with a decrease in the overall effective mass seen in the Γ–Z and Γ–N directions. This behavior also exists in LaCuOS and LaCuOSe, where a larger Cu–Cu distance is not detrimental to the conductivity, and transparency is observed for LaCuOS.[47,61] Of the predicted TCs, the lowest hole effective masses were seen for BaSc, making this the most promising discovery from this work.

For BaSc to be a successful *p*-type TC it would need to achieve large carrier concentrations from intrinsic defects such as vacancies and antisites (e.g., V_{Cu} or Sr_{Sc}) or through extrinsic doping. Judging from the conductivities found by Liu et al. of 2.8 S cm^{-1} for undoped powders of $[Cu_2S_2][Sr_3Sc_2O_5]$,[51] it is likely that shallow intrinsic acceptor defects could be present in the BaSc analog. A full analysis of the intrinsic defect chemistry, however, is beyond the scope of the present study due to the sheer number of defect types and charge states to consider. Speculation on the possible defects can be made by drawing parallels with an already studied layered oxychalcogenide, LaCuOSe. In this material, it was found that the intrinsic defects do not fully account for the high conductivities as the lowest formation energy acceptor, V_{Cu}, has a modest ionization energy of ~0.1 eV;[47] however, under *p*-type favorable growth conditions (a Se/O-rich regime) there is a relatively large dopability window where minimal compensation occurs. This explains the often reported *p*-type conductivity from Mg doping (~910 S cm^{-1}).[48] If a similar situation arises in BaSc, enhanced *p*-type conductivity can be expected by doping with group I cations, for example, without intrinsic or self-compensation.[5]

Additionally, the polaronic binding energy of holes can be calculated for BaSc and SrSc, giving rise to values of 0.04 eV and 0.08 eV, respectively, within the *ab* plane, categorizing them as type II compounds as per the convention defined by Davies et al.[69] It is clear that BaSc will be a better *p*-type conductor than SrSc, although while these values are slightly above any room-temperature excitation (~0.03 eV at k_BT at 300 K) it can be expected that excitation could occur from photons with wavelengths greater than mid-infrared (IR).[70]

It is also important to understand whether such carrier concentrations would be detrimental to the optical absorption. As such, transitions from below the VBM were calculated to simulate the effect of hole doping on the optical properties of BaSc using the method outlined by Scanlon and Watson.[37] The optical spectrum can be found in Figure S4 and shows that visible light absorption should in fact be negligible, with the significant transitions occurring in the near-IR, suggesting that BaSc will remain a transparent *p*-type conductor upon doping, similar to SrSc.[37]

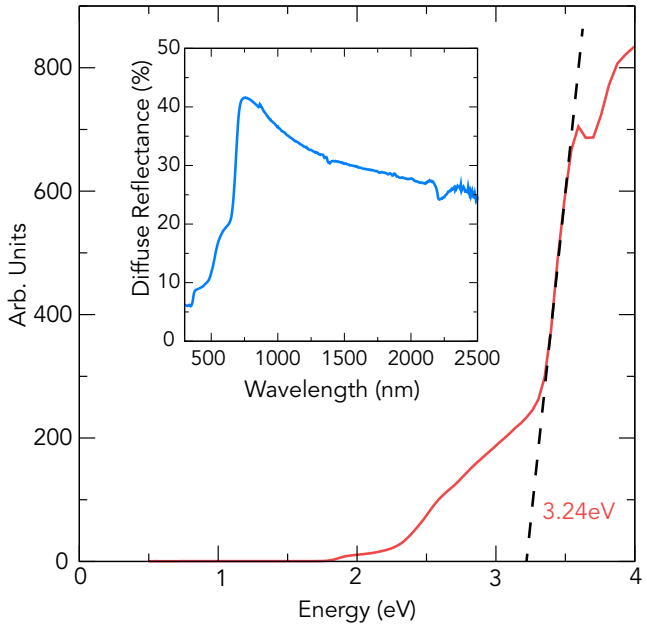

Figure 10. Tauc Plot, $[f(R)h\nu]^2$ versus Photon Energy, Derived from the Raw Diffuse Reflectance Spectrum (Inset) Collected Over a Range of 300–2,500 nm at Intervals of 5 nm

The dashed line extrapolated to the abscissa models the linear region of absorption edge for calculation of the band-gap energy.

Optimizing the band gap in the $[Cu_2S_2][A_3M_2O_5]$ layered oxychalcogenides is based upon two observations. Firstly, a smaller valence bandwidth could play a role in improving the magnitude of the band gap. In general it was seen that a larger Cu–Cu distance resulted in a smaller valence band width, which could explain the increase in band gap seen in the scandium compounds (where the CBM is not influenced by M^{3+} states). Secondly, the states that make up the CBM highly influence the position of the conduction band. In the aluminum and gallium compounds, the low-lying M^{3+} *s* states cause a sharp reduction in the band gap. The position of the conduction band is highly sensitive to the M^{3+}–O bond length; thus, larger cells push the CBM lower in energy. Despite this, because increasing the cell size reduces the VBM effective mass, a compromise is necessary for a wide-band-gap, high-mobility TC. In both the aluminum and scandium compounds there is significant mixing of the Cu and S states at the CBM, which could enhance the transparency that can be seen by the decrease in fundamental band gap with increasing percentage of Cu and S states at the CBM. The decrease in band gap in the aluminum compounds with increasing *a* is similar to that observed in other layered oxychalcogenides such as LaCuOSe (2.82 eV[17]), SmOCuSe (2.60 eV[71]), and YOCuSe (2.58 eV[72]), the reverse of which is observed in the $[Cu_2S_2][A_3Sc_2O_5]$ compounds.

From our analysis, four other compounds were found to be stable, albeit without band gaps wide enough to accommodate high optical transparencies. It is possible, however, that these materials could be used in other applications such as photovoltaics or photocatalysis. SrGa, for example, displays a band gap in the correct range for a solar absorber (E_g^{opt} = 1.71 eV),[73] yet despite this the optical absorption onset is fairly weak. It could be possible, however, to create an alloyed oxychalcogenide such as SrGa/BaGa or BaAl/BaGa to reduce the band gap or create a stronger absorption.[74] BaAl possesses a band gap in the range of a visible light water splitter[75] (2.42 eV), although the metastability of BaAl may be a limiting factor.

The thermodynamic stability of the compounds is likely restricted by certain structural parameters such as the volume, S–Cu–S bond angles, and Cu–S bond lengths; thus, going from S to Se to Te could help accommodate a smaller or larger cell size such as the Mg or La cells found to be unstable in this work. In the literature, the smallest analog found synthesized under atmospheric pressure is $[Cu_2S_2][Sr_3Fe_2O_5]$,[76] which possessed a volume of 402.69 $Å^3$; smaller volumes were attainable for $[Fe_2(P,As)_2][Ca_3Al_2O_5]$[77] (348.29 $Å^3$ and 365.16 $Å^3$, respectively), although these were synthesized at 4.5 GPa. These known limits could give rise to difficulties in atmospheric pressure synthesis of the Al compounds.

Comparing LaCuOS, LaCuOSe, and LaCuOTe, the S–Cu–S bond angles decrease from 111.2° → 107.5° → 103.5°, respectively; however, the Cu–S bond lengths increase from 2.42 Å → 2.52 Å → 2.66 Å, respectively.[66] It is expected that the VBM dispersion will increase down the chalcogenides as seen with the increased conductivity from LaCuOS to LaCuOSe.[47] Including Se and Te into the $[Cu_2S_2][A_3M_2O_5]$ structure, however, would likely reduce the band gap as well,[17,48,65,78] which is observed in other layered Cu–chalcogen structures such as BaFCuS (3.2 eV),[79] BaFCuSe (2.9 eV[80]), and BaFCuTe (2.3 eV[81]).[72] However, by combining the design rules laid out herein, transparency with a selenide or telluride may be possible, i.e., $[Cu_2Se_2][(Y/La)_2Al_2O_5]$. Other known layered Cu^{1+} oxychalcogenide structures such as $[CuS][Sr_2GaO_3]$,[82] $[Cu_2S_2][Bi_2YO_4]$,[83] or $[Cu_2S_2][Sr_2(Mn/Zn)O_2]$,[84,85] to name a few, could also be explored in the same way.

The prediction of a potential high-conductivity *p*-type TC has been achieved using a thermodynamic stability screening guided by chemical knowledge using DFT. Based on the $[Cu_2S_2][Sr_3Sc_2O_5]$ structure, 24 compounds were proposed, 8 of which were found to be stable and to possess semiconductor properties. The compound $[Cu_2S_2][Ba_3Sc_2O_5]$ was found to possess a wide optical band gap (E_g^{opt} = 3.24 eV) and high calculated *p*-type conductivities (~2,058 S cm^{-1}), which is in the conductivity range of thin films of industry standard *n*-type TCs and the largest predicted for any *p*-type TC. Synthesized powders of $[Cu_2S_2][Ba_3Sc_2O_5]$ confirmed the structural and optical properties predicted by hybrid DFT. This work paves the way for the design of higher-mobility *p*-type TCs, increasing the possibility of transparent electronics.

EXPERIMENTAL PROCEDURES

Resource Availability

Lead Contact

Benjamin A.D. Williamson (Computational), Geoffrey Hyett (Experimental).

Materials Availability

The new compound generated in this study can be synthesized from commercially available precursors, as detailed in Experimental Methods. However, we would be willing to share small quantities (~100 mg) of $[Cu_2S_2][Ba_3Sc_2O_5]$ upon request, with reasonable compensation by the requestor for materials costs, processing, and shipping.

Data and Code Availability

The HSE06 relaxed CIF files are given in an online Github repository found at https://github.com/SMTG-UCL/SCSOS or at Mendeley Data: https://doi.org/10.17632/2g3s8dttnb.1.

Please cite this article in press as: Williamson et al., Computationally Driven Discovery of Layered Quinary Oxychalcogenides: Potential *p*-Type Transparent Conductors?, Matter (2020), https://doi.org/10.1016/j.matt.2020.05.020

Computational Methods

Ab initio calculations using the VASP code[86–89] were performed using both standard and hybrid functionals. Variations of the $[Cu_2S_2][A_3M_2O_5]$ structure (tetragonal, I4/mmm) were formed where A = **Sr**,Ca,Ba,Mg and M = **Sc**,Al,Ga,In,Y,La. This resulted in 24 compounds with the same stoichiometry as $[Cu_2S_2][Sr_3Sc_2O_5]$ and are named using the convention "AB," e.g., $[Cu_2S_2][Sr_3Sc_2O_5]$ is "SrSc" and $[Cu_2S_2][Ba_3Al_2O_5]$ is "BaAl". These compounds were relaxed using the PBEsol[90] (Perdew-Burke-Ernzerhof revised for solids) functional with a Hubbard-like U correction value of 5.17 eV for Cu.[37] The projector-augmented wave method (PAW)[91] was used to describe the interactions between the core electrons and valence electrons, which are treated explicitly. The 24 compounds were relaxed using a plane-wave energy cutoff of 500 eV to avoid Pulay stress[92] and a 6 × 6 × 2 Γ-centered *k*-point mesh for accuracy. Convergence was deemed complete when the force acting on all the ions was less than 0.01 eV $Å^{-1}$.

To screen the compounds in terms of their thermodynamic stability, we also calculated all known competing phases and elements related to the quinary systems using PBEsol+U (Tables S1 and S2). This resulted in the calculation of ~313 crystal structures from the ICSD[59] alongside calculating the lowest energy magnetic orderings for each of the Cu^{2+}-containing compounds. A standard 500-eV plane-wave energy cutoff was employed to allow for total convergence of these systems together with *k*-point meshes generated to allow a sampling density of 0.04 $Å^{-1}$, which was found to be sufficiently accurate. The Chemical Potential Limits Analysis Program (CPLAP)[93] code was used to assess the thermodynamic stability of the 24 $[Cu_2S_2][A_3M_2O_5]$ compounds as well as evaluating the E above hull for the unstable compounds.

The stable and metastable compounds were then subjected to an HSE06 (Heyd-Scuzeria-Ernzerhof)[94] relaxation to glean accurate electronic and optical properties. The HSE06 hybrid functional has been shown to give a correct description of the band gap and optical properties of SCSOS[61] relative to experiment.[51] The optical absorption spectra were calculated using the real and imaginary parts of the dielectric constant calculated using a Kramers-Kronig transformation and a summation over the unoccupied bands, respectively, using a method by Furthmüller and coworkers.[95] This sums the absorption spectrum over all direct valence-band-to-conduction-band transitions ignoring intraband and indirect absorptions.

The effective masses of the valence and conduction band extrema are calculated using the relationship

$$\frac{1}{m^*_{ij}} = \frac{\delta^2 E(k)}{\delta k_i \delta k_j} \frac{1}{\hbar^2}, \qquad \text{(Equation 1)}$$

where $E(k)$ is defined as the eigenvalue of the band at a specific k and m^*_{ij} as the effective mass.

Phonon dispersions were calculated with Phonopy[96] using the finite displacement method and 3 × 3 × 2 supercells (252 atoms) generated from the optimized structure. The optimized structure was minimized using PBEsol with a force convergence criterion of 1×10^{-3} and the electronic wavefunction converged to 1×10^{-8}.

Electrical conductivity values were calculated using Boltzmann transport theory within the BoltzTraP[97] code. A dense Γ-centered 13 × 13 × 4 *k*-point mesh was

deemed sufficient for use (HSE06) within VASP, which can be read by BoltzTraP. The calculated conductivity represents a theoretical maximum with the scattering processes treated by the relaxation time approximation.

The polaron binding energy ($E_{polaron}$) can be calculated using the formalism laid out by Fröhlich:[70,98,99]

$$E_{polaron} = \frac{1}{8\pi^2}\frac{m^* e^4}{\hbar^2 \varepsilon_{eff}^2}, \quad \text{(Equation 2)}$$

where

$$\frac{1}{\varepsilon_{eff}} = \left(\frac{1}{\varepsilon_\infty} - \frac{1}{\varepsilon_0}\right) \quad \text{(Equation 3)}$$

and where ε_∞ and ε_0 are the optical high-frequency dielectric constant and the low dielectric constant, respectively.

The open-source Python package Sumo[100] (github.com/SMTG-UCL/sumo) by Ganose et al. was used in the production of the DOS, electronic band structures, effective masses, optical absorption, and phonon dispersion plots.

Experimental Methods

Solid-State Synthesis

Sc_2O_3 (99.99%, Alfa Aesar) and Cu_2S (99.5%, Alfa Aesar) were purchased and used as supplied. BaO was prepared via the thermal decomposition of $BaCO_3$ (99%. Alfa Aesar) under dynamic vacuum (1,000°C, 14 h) in a silica tube closed at one end before being stored in a nitrogen-filled glovebox (Saffron). BaS was synthesized by reaction of CS_2 vapor with $BaCO_3$ (900°C, 8 h). The CS_2 vapor was generated by flowing argon (Pureshield, 99.998%; BOC) through a bubbler containing liquid CS_2 (99.9%; Sigma-Aldrich). After the vapor exited the reactor, it was passed through two hydroxide-bleach containing bubblers to oxidize any excess CS_2 or H_2S. The purity of these precursors was confirmed by PXRD. A 0.5-g powder sample of $[Cu_2S_2][Ba_3Sc_2O_5]$ was synthesized by reaction of BaO, BaS, Sc_2O_3, and Cu_2S in a 2:1:1:1 stoichiometric ratio. Desired precursor amounts were weighed, mixed, and ground in an agate pestle and mortar under an inert atmosphere in a glovebox. The precursor mixture was then loaded into a die (13 mm, Specac), removed from the glovebox, pressed into a pellet, and immediately returned to the inert atmosphere. The pellet was loaded into an alumina crucible, which was then sealed under vacuum in a silica ampoule. The sealed sample was heat treated at 800°C for 12 h. The sample was ground, repelleted, and resealed in an alumina crucible in a silica ampoule with two further heat treatments at 800°C for 12 h. Sample purity was monitored using PXRD, and once synthesized the sample was found to be air stable by detection limits of lab PXRD.

X-Ray Diffraction

The purity of precursors and initial phase identification of the targeted product was confirmed by X-ray diffraction (XRD) using a Bruker D2 in Bragg-Brentano geometry with a Cu Kα X-ray source (20 kV; 10 mA). Full characterization of the compound $[Cu_2S_2][Ba_3Sc_2O_5]$ was performed using synchrotron XRD data collected from the I11 beamline, Diamond Light Source, using 15-keV X-rays (0.82603 Å) over a range $10 < 2\theta < 100°$, with a step size of 0.001° and with a scan rate of 2.5° min^{-1}. Rietveld refinement of structural models against these data was carried out using the GSAS suite of software with the EXPGUI interface.[101]

Spectrophotometry

Diffuse reflectance measurements were collected using a UV-visible near-IR spectrophotometer (PerkinElmer Lambda 750 S) using deuterium and tungsten lamps and equipped with a 100-mm integrating sphere. Diffuse reflectance data were converted into the Kubelka-Munk function, f(R),[102] assumed proportional to the absorption coefficient throughout the visible region, which was used in the construction of a Tauc plot.[103,104] The band gap was estimated by determining the *x*-axis intercept of a linear fit of the absorption edge. This was fitted by the plotting of a linear function passing through the two data points between which the largest gradient was observed.

SUPPLEMENTAL INFORMATION

Supplemental Information can be found online at https://doi.org/10.1016/j.matt.2020.05.020.

ACKNOWLEDGMENTS

B.A.D.W. would like to acknowledge useful discussions with Dr. A.M. Ganose, Dr. C.N. Savory, and Dr. D.W. Davies. B.A.D.W. would like to acknowledge Mr. K. Spooner for his assistance in the *n*-type TC BoltzTraP data. G.J.L. would like to acknowledge experimental support from Mr. D. Salazar-Marcano, Mr. P. Bayliss, and Mr. N. Davis. Thank you to Mr. C. Tang for performing the synchrotron diffraction experiment. G.J.L. and G.H. would also like to thank Prof. G. Reid and Prof. A. Hector, and Dr. D. Bradshaw and Dr. S. Cosham for useful discussions. This work made use of the ARCHER UK National Supercomputing Service (http://www.archer.ac.uk) via our membership of the UK's HEC Materials Chemistry Consortium, which is also funded by the EPSRC (EP/L000202). The UCL Legion and Grace HPC Facilities (Legion@UCL and Grace@UCL) were also used in the completion of this work. G.J.L. and G.H. would like to acknowledge support from the EPSRC (EP/T011793/1) and use of the Diamond I11 Rapid Access beamtime: EE16644. D.O.S. would like to acknowledge support from the EPSRC (EP/N01572X/1), and B.A.D.W. and D.O.S. would like to acknowledge support from the European Research Council (grant 758345). D.O.S. acknowledges membership of the Materials Design Network.

AUTHOR CONTRIBUTIONS

D.O.S. conceived the idea and designed the project; B.A.D.W. carried out all the computational simulations with the exception of the optical absorption calculations $[Cu_2S_2][Ba_3Sc_2O_5]$ with a hole in the valence band, which were performed by G.W.W.; G.J.L. and G.H. undertook all of the solid-state synthesis, spectroscopy, and analysis; B.A.D.W. submitted the manuscript and is the Lead Contact. All authors contributed to the writing of the manuscript and gave approval to the final version of the manuscript.

DECLARATION OF INTERESTS

The authors declare no competing interests.

Received: December 20, 2019
Revised: March 12, 2020
Accepted: May 20, 2020
Published: June 23, 2020

Please cite this article in press as: Williamson et al., Computationally Driven Discovery of Layered Quinary Oxychalcogenides: Potential *p*-Type Transparent Conductors?, Matter (2020), https://doi.org/10.1016/j.matt.2020.05.020

REFERENCES

1. Zhang, K.H.L., Xi, K., Blamire, M.G., and Egdell, R.G. (2016). P-type transparent conducting oxides. J. Phys. Condens. Matter *28*, 383002.

2. Fan, J.C.C., Bachner, F.J., and Foley, G.H. (1977). Effect of O_2 pressure during deposition on properties of RF-sputtered Sn-doped In_2O_3 films. Appl. Phys. Lett. *31*, 773–775.

3. Bhachu, D.S., Scanlon, D.O., Sankar, G., Veal, T.D., Egdell, R.G., Cibin, G., Dent, A.J., Knapp, C.E., Carmalt, C.J., and Parkin, I.P. (2015). Origin of high mobility in molybdenum-doped indium oxide. Chem. Mater. *27*, 2788–2796.

4. Oshima, M., and Yoshino, K. (2011). Characteristic of low resistivity fluorine-doped SnO_2 thin films grown by spray pyrolysis. Jpn. J. Appl. Phys. *50*, 05FB15.

5. Swallow, J.E.N., Williamson, B.A.D., Whittles, T.J., Birkett, M., Featherstone, T.J., Peng, N., Abbott, A., Farnworth, M., Cheetham, K.J., Warren, P., et al. (2017). Self-compensation in transparent conducting F-doped SnO_2. Adv. Funct. Mater. *28*, https://doi.org/10.1002/adfm.201701900.

6. Ponja, S.D., Williamson, B.A.D., Sathasivam, S., Scanlon, D.O., Parkin, I.P., and Carmalt, C.J. (2018). Enhanced electrical properties of antimony doped tin oxide thin films deposited via aerosol assisted chemical vapour deposition. J. Mater. Chem. C *6*, 7257–7266.

7. Powell, M.J., Williamson, B.A.D., Baek, S.-Y., Manzi, J., Potter, D.B., Scanlon, D.O., and Carmalt, C.J. (2018). Phosphorus doped SnO_2 thin films for transparent conducting oxide applications: synthesis, optoelectronic properties and computational models. Chem. Sci. *9*, 7968–7980.

8. Agura, H., Suzuki, A., Matsushita, T., Aoki, T., and Okuda, M. (2003). Low resistivity transparent conducting Al-Doped ZnO films prepared by pulsed laser deposition. Thin Solid Films *445*, 263–267.

9. Dixon, S.C., Sathasivam, S., Williamson, B.A.D., Scanlon, D.O., Carmalt, C.J., and Parkin, I.P. (2017). Transparent conducting n-type ZnO:Sc—synthesis, optoelectronic properties and theoretical insight. J. Mater. Chem. C *5*, 7585–7597.

10. Sallis, S., Scanlon, D.O., Chae, S.C., Quackenbush, N.F., Fischer, D.A., Woicik, J.C., Guo, J.-H., Cheong, S.W., and Piper, L.F.J. (2013). La-doped $BaSnO_3$—degenerate perovskite transparent conducting oxide: evidence from synchrotron X-ray spectroscopy. Appl. Phys. Lett. *103*, 042105.

11. Scanlon, D.O. (2013). Defect engineering of $BaSnO_3$ for high-performance transparent conducting oxide applications. Phys. Rev. B *87*, 161201.

12. Kawazoe, H., Yasukawa, M., Hyodo, H., Kurita, M., Yanagi, H., and Hosono, H. (1997). P-type electrical conduction in transparent thin films of $CuAlO_2$. Nature *389*, 939–942.

13. Hiramatsu, H., Ueda, K., Ohta, H., Hirano, M., Kamiya, T., and Hosono, H. (2003). Wide gap p-type degenerate semiconductor: Mg-doped LaCuOSe. Thin Solid Films *445*, 304–308.

14. Zakutayev, A., Paudel, T.R., Ndione, P.F., Perkins, J.D., Lany, S., Zunger, A., and Ginley, D.S. (2012). Cation off-stoichiometry leads to high p-type conductivity and enhanced transparency in Co_2ZnO_4 and Co_2NiO_4 thin films. Phys. Rev. B *85*, https://doi.org/10.1103/PhysRevB.85.085204.

15. Fan, J., Sreekanth, K., Xie, Z., Chang, S., and Rao, K. (2013). p-type ZnO materials: theory, growth, properties and devices. Prog. Mater. Sci. *58*, 874–985.

16. Williamson, B.A.D., Buckeridge, J., Brown, J., Ansbro, S., Palgrave, R.G., and Scanlon, D.O. (2016). Engineering valence band dispersion for high mobility p-type semiconductors. Chem. Mater. *29*, 2402–2413.

17. Hiramatsu, H., Ueda, K., Ohta, H., Hirano, M., Kamiya, T., and Hosono, H. (2003). Degenerate p-type conductivity in wide-gap $LaCuOS_{1-x}Se_x$ (x=0-1) epitaxial films. Appl. Phys. Lett. *82*, 1048–1050.

18. Mizoguchi, H., Hirano, M., Fujitsu, S., Takeuchi, T., Ueda, K., and Hosono, H. (2002). $ZnRh_2O_4$: a p-type semiconducting oxide with a valence band composed of a low spin state of Rh^{3+} in a $4d^6$ configuration. Appl. Phys. Lett. *80*, 1207–1209.

19. Brauer, G., Kuriplach, J., Ling, C.C., and Djurišić, A.B. (2011). Activities towards p-type doping of ZnO. J. Phys. Conf. Ser. *265*, 012002.

20. Suja, M., Bashar, S.B., Morshed, M.M., and Liu, J. (2015). Realization of Cu-doped p-type ZnO thin films by molecular beam epitaxy. ACS Appl. Mater. Interfaces *7*, 8894–8899.

21. Pan, H., Meng, X., Cai, J., Li, S., and Qin, G. (2015). 4d transition-metal doped hematite for enhancing photoelectrochemical activity: theoretical prediction and experimental confirmation. RSC Adv. *5*, 19353–19361.

22. Tsay, C.-Y., and Liang, S.-C. (2015). Fabrication of p-type conductivity in SnO_2 thin films through Ga doping. J. Alloys Compd. *622*, 644–650.

23. Pan, S.S., Li, G.H., Wang, L.B., Shen, Y.D., Wang, Y., Mei, T., and Hu, X. (2009). Atomic nitrogen doping and p-type conduction in SnO_2. Appl. Phys. Lett. *95*, 222112.

24. Pan, S.S., Wang, S., Zhang, Y.X., Luo, Y.Y., Kong, F.Y., Xu, S.C., Xu, J.M., and Li, G.H. (2012). P-type conduction in nitrogen-doped SnO_2 films grown by thermal processing of tin nitride films. Appl. Phys. A *109*, 267–271.

25. Asbalter, J., and Subrahmanyam, A. (2000). P-type transparent conducting In_2O_3-Ag_2O thin films prepared by reactive electron beam evaporation technique. J. Vac. Sci. Technol. A *18*, 1672–1676.

26. Li, Y., Sun, J., and Singh, D.J. (2017). Infrared absorption and visible transparency in heavily doped p-type $BaSnO_3$. Appl. Phys. Lett. *110*, 051904.

27. Hsin, C.L., He, J.H., Lee, C.Y., Wu, W.W., Yeh, P.H., Chen, L.J., and Wang, Z.L. (2007). Lateral self-aligned p-type In_2O_3 nanowire arrays epitaxially grown on Si substrates. Nano Lett. *7*, 1799–1803.

28. Perkins, J.D., Paudel, T.R., Zakutayev, A., Ndione, P.F., Parilla, P.A., Young, D.L., Lany, S., Ginley, D.S., Zunger, A., Perry, N.H., et al. (2011). Inverse design approach to hole doping in ternary oxides: enhancing p-type conductivity in cobalt oxide spinels. Phys. Rev. B *84*, 205207.

29. Kim, H.J., Song, I.C., Sim, J.H., Kim, H., Kim, D., Ihm, Y.E., and Choo, W.K. (2004). Electrical and magnetic properties of spinel-type magnetic semiconductor $ZnCo_2O_4$ grown by reactive magnetron sputtering. J. Appl. Phys. *95*, 7387–7389.

30. Kawazoe, H., Yanagi, H., Ueda, K., and Hosono, H. (2000). Transparent p-type conducting oxides: design and fabrication of p-n heterojunctions. MRS Bull. *25*, 28–36.

31. Ievtushenko, A., Khyzhun, O., Shtepliuk, I., Bykov, O., Jakieła, R., Tkach, S., Kuzmenko, E., Baturin, V., Karpenko, O., Olifan, O., et al. (2017). X-ray photoelectron spectroscopy study of highly-doped ZnO:Al,N films grown at O-rich conditions. J. Alloys Compd. *722*, 683–689.

32. Marquardt, M.A., Ashmore, N.A., and Cann, D.P. (2006). Crystal chemistry and electrical properties of the delafossite structure. Thin Solid Films *496*, 146–156.

33. Ueda, K., Hase, T., Yanagi, H., Kawazoe, H., Hosono, H., Ohta, H., Orita, M., and Hirano, M. (2001). Epitaxial growth of transparent *p*-type conducting $CuGaO_2$ thin films on sapphire (001) substrates by pulsed laser deposition. J. Appl. Phys. *89*, 1790–1793.

34. Miao, M.-S., Yarbro, S., Barton, P.T., and Seshadri, R. (2014). Electron affinities and ionization energies of Cu and Ag delafossite compounds: a hybrid functional study. Phys. Rev. B *89*, 045306.

35. Kandpal, H.C., and Seshadri, R. (2002). First-principles electronic structure of the delafossites ABO_2 (A = Cu, Ag, Au; B = Al, Ga, Sc, in, Y): evolution of d^{10}-d^{10} interactions. Solid State Sci. *4*, 1045–1052.

36. Nagarajan, R., Draeseke, A.D., Sleight, A.W., and Tate, J. (2001). p-type conductivity in $CuCr_{1-x}Mg_xO_2$ films and powders. J. Appl. Phys. *89*, 8022–8025.

37. Scanlon, D.O., and Watson, G.W. (2009). $Cu_2S_2)(Sr_3Sc_2O_5)$—a layered, direct band gap, *p*-type transparent conducting oxychalcogenide: a theoretical analysis. Chem. Mater. *21*, 5435–5442.

38. Snure, M., and Tiwari, A. (2007). $CuBO_2$: A *p*-type transparent oxide. Appl. Phys. Lett. *91*, https://doi.org/10.1063/1.2778755.

39. Shi, L.-J., Fang, Z.-J., and Li, J. (2008). First-principles study of p-type transparent conductive oxides CuXOsub [2] (X=Y, Sc, and Al). J. Appl. Phys. *104*, 073527.

40. Godinho, K.G., Carey, J.J., Morgan, B.J., Scanlon, D.O., and Watson, G.W. (2010).

Understanding conductivity in $SrCu_2O_2$: stability, geometry and electronic structure of intrinsic defects from first principles. J. Mater. Chem. *20*, 1086.

41. Kudo, A., Yanagi, H., Hosono, H., and Kawazoe, H. (1998). $SrCu_2O_2$: a *p*-type conductive oxide with wide band gap. Appl. Phys. Lett. *73*, https://doi.org/10.1063/1.121761.

42. Scanlon, D.O., and Watson, G.W. (2010). Conductivity limits in $CuAlO_2$ from screened-hybrid density functional theory. J. Phys. Chem. Lett. *1*, 3195–3199.

43. Scanlon, D.O., and Watson, G.W. (2011). Understanding the *p*-type defect chemistry of $CuCrO_2$. J. Mater. Chem. *21*, 3655.

44. Kashida, S., Shimosaka, W., Mori, M., and Yoshimura, D. (2003). Valence band photoemission study of the copper chalcogenide compounds, Cu_2S, Cu_2Se and Cu_2Te. J. Phys. Chem. Sol. *64*, 2357–2363.

45. Wu, Y., Wadia, C., Ma, W., Sadtler, B., and Alivisatos, A.P. (2008). Synthesis and photovoltaic application of copper(I) sulfide nanocrystals. Nano Lett. *8*, 2551–2555.

46. Scanlon, D.O., Godinho, K.G., Morgan, B.J., and Watson, G.W. (2010). Understanding conductivity anomalies in Cu-based delafossite transparent conducting oxides: theoretical insights. J. Chem. Phys. *132*, 024707.

47. Scanlon, D.O., Buckeridge, J., Catlow, C.R.A., and Watson, G.W. (2014). Understanding doping anomalies in degenerate *p*-type semiconductor LaCuOSe. J. Mater. Chem. C *2*, 3429–3438.

48. Hiramatsu, H., Ueda, K., Ohta, H., Hirano, M., Kikuchi, M., Yanagi, H., Kamiya, T., and Hosono, H. (2007). Heavy hole doping of epitaxial thin films of a wide gap *p*-type semiconductor, LaCuOSe, and analysis of the effective mass. Appl. Phys. Lett. *91*, 012104.

49. Ueda, K., Inoue, S., Hirose, S., Kawazoe, H., and Hosono, H. (2000). Transparent *p*-type semiconductor: LaCuOS layered oxysulfide. Appl. Phys. Lett. *77*, 2701.

50. Otzschi, K., Ogino, H., Shimoyama, J.-i., and Kishio, K. (1999). New candidates for superconductors ; a series of layered oxysulfides $(Cu_2S_2)(Sr_{n+1}MnO_{3n-1})$. J. Low Temp. Phys. https://doi.org/10.1023/A:1022545228168.

51. Liu, M.-L., Wu, L.-B., Huang, F.-Q., Chen, L.-D., and Chen, I.-W. (2007). A promising p-type transparent conducting material: layered oxysulfide $[Cu_2S_2][Sr_3Sc_2O_5]$. J. Appl. Phys. *102*, 116108.

52. Xu, J., Liu, J.-B., Wang, J., Liu, B.-X., and Huang, B. (2018). Prediction of novel p-type transparent conductors in layered double perovskites: a first-principles study. Adv. Func. Mater. *28*, 1800332.

53. Hautier, G., Miglio, A., Ceder, G., Rignanese, G.-M., and Gonze, X. (2013). Identification and design principles of low hole effective mass p-type transparent conducting oxides. Nat. Commun. *4*, 2292.

54. Ha, V.-A., Yu, G., Ricci, F., Dahliah, D., van Setten, M.J., Giantomassi, M., Rignanese, G.-M., and Hautier, G. (2019). Computationally driven high-throughput identification of CaTe and Li_3Sb as promising candidates for high-mobility p -type transparent conducting materials. Phys. Rev. Mater. *3*, 034601.

55. Palgrave, R.G., Borisov, P., Dyer, M.S., McMitchell, S.R.C., Darling, G.R., Claridge, J.B., Batuk, M., Tan, H., Tian, H., Verbeeck, J., et al. (2012). Artificial construction of the layered Ruddlesden-Popper manganite $La_2Sr_2Mn_3O_{10}$ reflection high energy electron diffraction monitored pulsed laser deposition. J. Am. Chem. Soc. *134*, 7700–7714.

56. Haeni, J.H., Theis, C.D., Schlom, D.G., Tian, W., Pan, X.Q., Chang, H., Takeuchi, I., and Xiang, X.-D. (2001). Epitaxial growth of the first five members of the $Sr_{n+1}Ti_nO_{3n+1}$ Ruddlesden-Popper homologous series. Appl. Phys. Lett. *78*, 3292.

57. Tian, W., Pan, X.Q., Haeni, J.H., and Schlom, D.G. (2001). Transmission electron microscopy study of n=1-5 $Sr_{n+1}Ti_nO_{3n+1}$ epitaxial thin films. J. Mater. Res. *16*, 2013–2026.

58. Sayers, R., Flack, N.L.O., Alaria, J., Chater, P.A., Palgrave, R.G., McMitchell, S.R.C., Romani, S., Ramasse, Q.M., Pennycook, T.J., and Rosseinsky, M.J. (2013). Epitaxial growth and enhanced conductivity of an IT-SOFC cathode based on a complex perovskite superstructure with six distinct cation sites. Chem. Sci. *4*, 2403.

59. Bergerhoff, G., Brown, I., and Allen, F. (1987). Crystallographic Databases (International Union of Crystallography).

60. Sun, W., Dacek, S.T., Ong, S.P., Hautier, G., Jain, A., Richards, W.D., Gamst, A.C., Persson, K.A., and Ceder, G. (2016). The thermodynamic scale of inorganic crystalline metastability. Sci. Adv. *2*, e1600225.

61. Scanlon, D.O., Walsh, A., and Watson, G.W. (2009). Understanding the *p*-type conduction properties of the transparent conducting oxide $CuBO_2$: a density functional theory analysis. Chem. Mater. *21*, 4568–4576.

62. Evans, H.T. (1979). The crystal structures of low chalcocite and djurleite. Z. Kristallogr. *150*, 299–320.

63. Cava, R., Reidinger, F., and Wuensch, B. (1981). Mobile ion distribution and anharmonic thermal motion in fast ion conducting Cu_2S. Solid State Ionics *5*, 501–504.

64. Ueda, K., and Hosono, H. (2002). Crystal structure of $LaCuOS_{1-x}Se_x$ oxychalcogenides. Thin Solid Films *411*, 115–118.

65. Liu, M.L., Wu, L.B., Huang, F.Q., Chen, L.D., and Ibers, J.A. (2006). Syntheses, crystal and electronic structure, and some optical and transport properties of LnCuOTe (Ln=La, Ce, Nd). J. Solid State Chem. *180*, 62–69.

66. Ueda, K., Hosono, H., and Hamada, N. (2004). Energy band structure of LaCuOCh (Ch = S, Se and Te) calculated by the full-potential linearized augmented plane-wave method. J. Phys. Condens. Matter *16*, 5179–5186.

67. Lyons, J.L., Janotti, A., and de Walle, C.G.V. (2014). Effects of carbon on the electrical and optical properties of InN, GaN, and AlN. Phys. Rev. B *89*, 035204.

68. Fuchs, F., and Bechstedt, F. (2008). Indium-oxide polymorphs from first principles: quasiparticle electronic states. Phys. Rev. B *77*, 155107.

69. Davies, D.W., Savory, C.N., Frost, J.M., Scanlon, D.O., Morgan, B.J., and Walsh, A. (2020). Descriptors for electron and hole charge carriers in metal oxides. J. Phys. Chem. Lett. *11*, 438–444.

70. Pastor, E., Park, J.-S., Steier, L., Kim, S., Grätzel, M., Durrant, J.R., Walsh, A., and Bakulin, A.A. (2019). In situ observation of picosecond polaron self-localisation in α-Fe_2O_3 photoelectrochemical cells. Nat. Commun. *10*, 3962.

71. Llanos, J., and Peña, O. (2005). Electrical resistivity, optical and magnetic properties of the layered oxyselenide SmCuOSe. J. Solid State Chem. *178*, 957–960.

72. Clarke, S.J., Adamson, P., Herkelrath, S.J.C., Rutt, O.J., Parker, D.R., Pitcher, M.J., and Smura, C.F. (2008). Structures, physical properties, and chemistry of layered oxychalcogenides and oxypnictides. Inorg. Chem. *47*, 8473–8486.

73. Ganose, A.M., Savory, C.N., and Scanlon, D.O. (2017). Beyond methylammonium lead iodide: prospects for the emergent field of ns^2 containing solar absorbers. Chem. Commun. *53*, 20–44.

74. Ganose, A.M., and Scanlon, D.O. (2016). Band gap and work function tailoring of SnO_2 for improved transparent conducting ability in photovoltaics. J. Mater. Chem. C *4*, 1467–1475.

75. Walsh, A., Ahn, K.-S., Shet, S., Huda, M.N., Deutsch, T.G., Wang, H., Turner, J.A., Wei, S.-H., Yan, Y., and Al-Jassim, M.M. (2009). Ternary cobalt spinel oxides for solar driven hydrogen production: theory and experiment. Energy Environ. Sci. *2*, 774.

76. Zhu, W., and Hor, P. (1997). Crystal structure of new layered oxysulfides: $Sr_3Cu_2Fe_2O_5S_2$ and Sr_2CuMO_3S (M=Cr, Fe, In). J. Solid State Chem. *134*, 128–131.

77. Shirage, P.M., Kihou, K., Lee, C.-H., Kito, H., Eisaki, H., and Iyo, A. (2011). Emergence of superconductivity in "32522" structure of $(Ca_3Al_2O_5$-y$)(Fe_2Pn_2)$ (Pn = As and P). J. Am. Chem. Soc. *133*, 9630–9633.

78. Hiramatsu, H., Ueda, K., Takafuji, K., Ohta, H., Hirano, M., Kamiya, T., and Hosono, H. (2003). Intrinsic excitonic photoluminescence and band-gap engineering of wide-gap p-type oxychalcogenide epitaxial films of LnCuOCh (Ln=La, Pr, and Nd: Ch=S or Se) semiconductor alloys. J. Appl. Phys. *94*, 5805–5808.

79. Yanagi, H., Park, S., Draeseke, A., Keszler, D., and Tate, J. (2003). P-type conductivity in transparent oxides and sulfide fluorides. J. Solid State Chem. *175*, 34–38.

80. Park, C.-H., Keszler, D.A., Yanagi, H., and Tate, J. (2003). Gap modulation in $MCu[Q_{1-x}Q'_x]F$ (M=Ba, Sr: Q, Q'=S, Se, Te)

and related materials. Thin Solid Films *445*, 288–293.

81. Park, C.-H., Kykyneshi, R., Yokochi, A., Tate, J., and Keszler, D.A. (2007). Structure and physical properties of BaCuTeF. J. Solid State Chem. *180*, 1672–1677.

82. Zhu, W.J., and Hor, P.H. (1997). Sr_2CuGaO_3S, a rare example of square pyramidal gallium. Inorg. Chem. *36*, 3576–3577.

83. Evans, J.S.O., Brogden, E.B., Thompson, A.L., and Cordiner, R.L. (2002). Synthesis and characterisation of the new oxyselenide $Bi_2YO_4Cu_2Se_2$. Chem. Commun. 912–913.

84. Zhu, W., and Hor, P. (1997). Unusual layered transition-metal oxysulfides: $Sr_2Cu_2MO_2S_2$ (M=Mn, Zn). J. Solid State Chem. *130*, 319–321.

85. Hirose, H., Ueda, K., Kawazoe, H., and Hosono, H. (2002). Electronic structure of $Sr_2Cu_2ZnO_2S_2$ layered oxysulfide with CuS layers. Chem. Mater. *14*, 1037–1041.

86. Kresse, G., and Hafner, J. (1993). *Ab-initio* molecular dynamics for liquid metals. Phys. Rev. B *47*, 558–561.

87. Kresse, G., and Hafner, J. (1994). *Ab initio* molecular-dynamics simulation of the liquid-metal-amorphous-semiconductor transition in germanium. Phys. Rev. B *49*, 14251.

88. Kresse, G., and Furthmüller, J. (1996). Efficient iterative schemes for *ab initio* total-energy calculations using a plane-wave basis set. Phys. Rev. B *54*, 11169.

89. Kresse, G., and Furthmüller, J. (1996). Efficiency of *ab-initio* total energy calculations for metals and semiconductors using a plane-wave basis set. Comput. Mater. Sci. *6*, 15–50.

90. Perdew, J.P., Ruzsinszky, A., Csonka, G.I., Vydrov, O.A., Scuseria, G.E., Constantin, L.A., Zhou, X., and Burke, K. (2008). Restoring the density-gradient expansion for exchange in solids and surfaces. Phys. Rev. Lett. *100*, 136406.

91. Blochl, P. (1994). Projector augmented-wave method. Phys. Rev. B *50*, 17953–17979.

92. Pulay, P. (2002). Ab initio calculation of force constants and equilibrium geometries in polyatomic molecules. I. Theory (reprinted from Molecular Physics, vol 17, pg 197-204, 1969). Mol. Phys. *100*, 57–62.

93. Buckeridge, J., Scanlon, D.O., Walsh, A., and Catlow, C.R.A. (2014). Automated procedure to determine the thermodynamic stability of a material and the range of chemical potentials necessary for its formation relative to competing phases and compounds. Comput. Phys. Commun. *185*, 330–338.

94. A.V. Krukau, O.A. Vydrov, A.F. Izmaylov, G.E. Scuseria, Influence of the exchange screening parameter on the performance of screened hybrid functionals J. Chem. Phys. 125, 224106.

95. Adolph, B., Furthmüller, J., and Bechstedt, F. (2001). Optical properties of semiconductors using projector-augmented waves. Phys. Rev. B *63*, 125108.

96. Togo, A., and Tanaka, I. (2015). First principles phonon calculations in materials science. Scr. Mater. *108*, 1–5.

97. Madsen, G.K., and Singh, D.J. (2006). BoltzTraP. A code for calculating band-structure dependent quantities. Comput. Phys. Commun. *175*, 67–71.

98. Fröhlich, H. (1954). Electrons in lattice fields. Adv. Phys. *3*, 325–361.

99. Davies, D., Savory, C., Frost, J.M., Scanlon, D., Morgan, B., and Walsh, A. (2019). Descriptors for electron and hole charge carriers in metal oxides. ChemRxiv. https://doi.org/10.26434/chemrxiv.11214914.v1.

100. Ganose, A.M., Jackson, A.J., and Scanlon, D.O. (2018). Sumo: command-line tools for plotting and analysis of periodic Ab-initio calculations. J. Open Source Softw. *3*, 717.

101. Toby, B.H. (2001). EXPGUI, a graphical user interface for GSAS. J. Appl. Crystallogr. *34*, 210–213.

102. Kubelka, P. (1948). New contributions to the optics of intensely light-scattering materials part I. J. Opt. Soc. America *38*, 448.

103. Tauc, J., Grigorovici, R., and Vancu, A. (1966). Optical properties and electronic structure of amorphous germanium. Phys. Status Solidi (b) *15*, 627–637.

104. Tauc, J. (1968). Optical properties and electronic structure of amorphous Ge and Si. Mater. Res. Bull. *3*, 37–46.